Design and Analysis of MEMS-Based Metamaterials

by

Jonathan S. Varsanik

Submitted to the Department of Electrical Engineering and Computer Science
in partial fulfillment of the requirements for the degree of

Master of Engineering in Electrical Engineering and Computer Science

at the

MASSACHUSETTS INSTITUTE OF TECHNOLOGY

June 2006

Author .....
Department of Electrical Engineering and Computer Science
May 26, 2006

Certified by .....
Amy Duwel
Charles Stark Draper Laboratory Thesis Supervisor

Certified by .....
I-Au Kong
Supervisor

Accepted by ....
C. Smith
Chairman, Department Committee on Graduate Students

Design and Analysis of MEMS-Based Metamaterials

by

Jonathan S. Varsanik

Submitted to the Department of Electrical Engineering and Computer Science
on May 26, 2006, in partial fulfillment of the
requirements for the degree of
Master of Engineering in Electrical Engineering and Computer Science

Abstract

Metamaterials, materials that are constructed with arrays of small elements have significant potential to provide material properties that are useful for electromagnetic applications but are not found in nature. Slight changes to a repeated unit cell can be used to tune the effective bulk material properties of a metamaterial, replacing the need to discover suitable materials for an application with the ability to design a structure for the desired effect. However, most current metamaterial realizations are plagued by high loss, large size, awkward structure, or difficult construction. The use of Micro-Electro-Mechanical Systems (MEMS) to create a new metamaterial could improve upon some of these shortcomings due to their small size, high Q, and ease of integration into standard applications and circuit fabrication techniques. In this thesis, I analyze the prospects of a MEMS-based metamaterial. First, I determine the best type of MEMS resonator to use in a metamaterial. Then, I build models that can accurately describe a metamaterial constructed of MEMS unit cells. Analysis of these models provides information about the potential behavior of a MEMS metamaterial. It is discovered that it is possible to create a left-handed metamaterial using MEMS resonators. Finally, phase-shifting and antenna miniturization applications are suggested as potential areas that can leverage the benefits of this new MEMS metamaterial.

Charles Stark Draper Laboratory Thesis Supervisor: Amy Duwel

M.I.T. Thesis Supervisor: Jin-Au Kong

Acknowledgments

I would like to thank my Draper Supervisor, Dr. Amy Duwel for all her help throughout the entire year. Also at Draper, James Kang, James Hsiao, John Lachapelle, and Doug White, all had knowledge to offer in the course of this thesis. At MIT, my Thesis Advisor, Professor Jin Au Kong, along with Dr. Bae-Ian Wu provided a great wealth of knowledge in the area of metamaterials and electromagnetics that I wish I had given more consultation.

Personally, I would like to thank my girlfriend Catherine for making sure that I ate well, my mother for putting up with me, and my father for looking over me.

Thank you all.

This thesis was prepared at The Charles Stark Draper Laboratory, Inc., under Internal Company Sponsored Research and Development Project 20301-001, Miniature Antenna Technology.

Publication of this thesis does not constitute approval by Draper of the findings or conclusions contained herein. It is published for the exchange and stimulation of ideas.

Jonathan S. Varsanik

THIS PAGE INTENTIONALLY LEFT BLANK

Contents

THIS PAGE INTENTIONALLY LEFT BLANK

List of Figures

THIS PAGE INTENTIONALLY LEFT BLANK

List of Tables

THIS PAGE INTENTIONALLY LEFT BLANK

Chapter 1

Introduction

The term "metamaterial" refers to any material that is artificially constructed for the purpose of achieving desired properties. In electromagnetics, a metamaterial can be created by constructing a periodic structure with elements of size less than the wavelength of the incoming electromagnetic wave. Because the bulk properties of this material no longer depend on the materials used, but depend on the geometry of the structure, the resulting material can be engineered for any purpose, and can even achieve behaviors that are not found in nature.

The material values of particular interest to the electromagnetics community are the values of permittivity, ϵ, and permeability, μ. These values are a characterization of the ability of electric and magnetic fields, respectively, to polarize the medium. Taken together, ϵ and μ determine the speed of electromagnetic propagation through a medium, as well as many other important values. Through the use of metamaterials, we can create materials with chosen values for ϵ and μ, giving designers great control over the many material parameters that depend on those values.

While metamaterials may offer many exciting opportunities in electromagnetics, they also have several drawbacks. Depending on the type of metamaterial, there are problems with large physical size, significant loss, difficult system integration, and low bandwidth. Micro-Electro-Mechanical Systems (MEMS) devices boast small size and easy integration into current circuit fabrication techniques and may therefore provide a solution to some of these problems. In this thesis, I explore the use of

MEMS resonators to create a metamaterial. Also, I explore some potential uses for this metamaterial.

1.1 Overview of Chapters

The remainder of this chapter serves as an overview of the relevant work in the field of electromagnetic metamaterials. Additionally, existing metamaterial applications are discussed. An introduction to MEMS technology follows.

Chapter 2 performs an analysis of two types of MEMS resonator: the paddle and the piezoelectric resonators. Models of each resonator are built and optimized according to specific criteria. The integrity of a signal that is passed through each resonator is determined and compared. The preferred resonator is determined through these criteria, and will become the basic component for the metamaterials designed throughout the remainder of the thesis.

The following chapter, Chapter 3, is dedicated to the evaluation of the dispersion behavior of a MEMS metamaterial. First, a circuit model is constructed that recreates the behavior of the resonator. Using this model, a method for determining the dispersion relation through an arbitrary structure containing the resonator is constructed. Various structures are simulated and their results are compared. The simulation results are also compared to data obtained from a fabricated structure. Finally, one application for the use of the MEMS metamaterial as a phase shifting element is considered.

After the dispersion analysis, Chapter 4 explores the bulk material parameters that are potentially achievable through the use of a MEMS metamaterial. To determine these parameters, a model of the material must be created, and a method for extracting the material values is selected and refined. In order to determine the range of potential material parameters that can be achieved, the dimensions of the resonators used in the model are varied and the results are considered. A method is then introduced by which a designer can create a material with a chosen permittivity and permeability at a specific frequency. Finally, several applications of this new

material and the new design process are considered.

The final chapter is the conclusion. The conclusion reviews what was accomplished in the thesis. Also, the conclusion analyzes the potential of the applications presented and proposes directions for future work.

Following the conclusion is the Appendix. The Appendix contains two mathematical operations that were too large to be included in the main body of the thesis, but provided necessary results for my work. Specifically, the Appendix includes the conformal mapping of a microstrip line to a coplanar waveguide and the calculation of the torque acting on an electrostatically-actuated MEMS cantilever.

1.2 Left-Handed Metamaterials

The idea of a material with simultaneously negative values of permittivity, ϵ, and permeability, μ was initially presented by Veselago in 1968 [38]. When he was considering the definitions of the dispersion relation and index of refraction in an isotropic medium, which depend on the product and the quotient of μ and ϵ, Veselago conjectured that a simultaneous change of the signs of both ϵ and μ in a medium would have no effect on those relations. Furthermore, in a monochromatic wave, the Maxwell equations and the constitutive equations reduce to Equations 1.1 and 1.2.

$$[\bar{k}\bar{E}] = \frac{\omega}{c}\mu\bar{H} \tag{1.1}$$

$$[\bar{k}\bar{H}] = -\frac{\omega}{c}\epsilon\bar{E} \tag{1.2}$$

From Equations 1.1 and 1.2, we see that the wavevector is real. Recall that the wavevector describes the propagation of the wave in a medium. A real wavevector indicates a propagating wave, while an imaginary wavevector indicates attenuation (an evanescent wave). Therefore because the wavevector in Equations 1.1 and 1.2 is real, electromagnetic radiation is able to move through a material with these values. However, because the wavevector in those equations is negative, the material exhibits

interesting properties. The index of refraction, defined as $\sqrt{\epsilon\mu}$ will take the negative root. The phase velocity, defined as $\frac{\omega}{k}$ is also negative while the group velocity, $\frac{d\omega}{dk}$ is still positive. This difference in signs is one of the most interesting properties of left-handed materials. Because the group and phase velocities have opposite signs they are antiparallel, indicating that wave fronts move towards a source in this material creating a "backwards wave". However, because the Poynting vector, which is defined $E \times H$[1], is still positive, power travels away from the source and causality is maintained.

Due to the negative index of refraction, these materials are often referred to as NIMs (Negative Index of Refraction Materials). However, in this project, I will refer to them as "left-handed metamaterials" (LHMs), emphasizing the left-handed relationship between the electric field, the magnetic field, and the wavevector.

Until recently the study of left-handed materials was merely a thought exercise. However, recent advances in manufacturing technologies make it possible to construct metamaterials that can achieve this behavior. The first work in this direction was by Pendry. He created a medium consisting of thin wires arranged in a periodic array [32]. These wires acted as a plasma medium, whereby ϵ varies with frequency, following the relation of Equation 1.3, where ω_p is the plasma frequency and γ is a damping term, both of which are material properties. The value of ϵ was observed to and became negative at some frequencies.

$$\epsilon(\omega) = 1 - \frac{\omega_p^2}{\omega(\omega + i\gamma)} \tag{1.3}$$

Pendry next achieved a negative μ with a periodic array of metallic loops called Split Ring Resonators[31]. In a medium composed of these rings the permeability, μ, varied with frequency, and could become negative. In 1999, Smith combined the rod and ring materials to finally produce a material with simultaneously negative ϵ and μ, a left-handed material [35]. The left-handed behavior (specifically, the negative index of refraction) of this structure was experimentally verified by Shelby, Smith and

[1]With complex E and H, it should be E cross the complex conjugate of H, but that designation is omitted here for simplicity

Schultz [34].

The rod and ring material creates a negative index of refraction because the periodic elements are resonant structures. At specific frequencies, the resonators may fall at integral points along an incoming wavelength. The rod and ring element then stores and radiates energy at its own characteristic frequency, modifying the waveform. In the proper configuration, the energy storage and radiation of each element will interfere to produce the observed left handed effect.

Due to the complex nature of the rod and ring metamaterial, adjustment and further analysis proved difficult. The complicated geometry and behavior required sophisticated modeling techniques and was difficult to adjust for desired parameters. A more intuitive interpretation of the material was required. Because the rod and ring element behaved as a simple resonating element, the material was therefore modeled as an array of lumped circuit elements. The split-ring resonator was abstraced to a model as a circuit consisting of resistors, capacitors, and inductors [18]. This enabled the materials to be analyzed as a circuit, which was a familiar problem with simple solutions. Also, this abstraction made it easier to discern how changes in individual elements would change the global behavior of the medium.

The circuit model of the metamaterial, however, does not necessarily produce intuitive results for guided wave applications. Also, the modeling of an entire periodic array was redundant. A further abstraction was needed. It was recognized that different geometries of transmission line can reproduce the behavior of circuit elements and that wave propagation through a transmission line is an intuitive analog to wave propagation through a material. As a result, metamaterials have recently been analyzed using a transmission line model. Additionally, a left-handed metamaterial was constructed using transmission lines [8].

When creating transmission lines, the permittivity and permeability of the substrate material are important, as they determine the velocity of propagation, $v = (\epsilon\mu)^{-.5}$ and the impedance, $z = \sqrt{\frac{\mu}{\epsilon}}$. These two material parameters are also very important in antenna design because it is important to match the impedance of the feed to the antenna to that of its source. Also, a well-matched substrate impedance

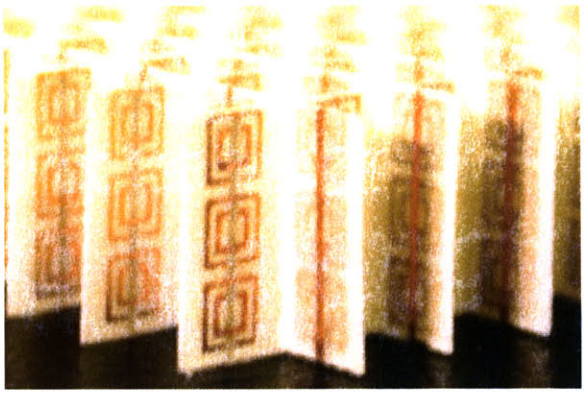

Figure 1-1: 2D rod and split ring resonator metamaterial. Taken from [34]

will couple well to the air, and radiate efficiently. For these reasons, models of metamaterial structure parameters are also further abstracted to produce effective values of ϵ and μ.

1.2.1 Existing Left-Handed Metamaterials

The rod and split ring medium built first by Smith is constructed from copper patterns on standard printed circuit board material. To make the two dimensional array that was used for verification, these units were arranged in a grid. A picture of this medium is shown in Figure 1-1. A prism-like shape was built with this grid to verify the left-handed behavior. Radiation was directed at the prism such that the wavevector of the incident waves was perpendicular to a face of the prism. After the radiation traveled through the prism and reached the angled interface with air, the nature of the medium would be revealed. By snell's law, $n_1 \sin\theta_1 = n_2 \sin\theta_2$. If the medium is right-handed, the angle that the wavevector of the emerging radiation makes with the normal vector of the face is positive, but, if the medium is left-handed, the angle is negative. The experiment was performed with radiation at a frequency of 10.5 GHz, and an index of refraction of -2.7 was observed [34].

The metamaterial constructed for the experiment by Shelby et. al. had some limitations due to the frequency range of the elements that they were using. When the index of refraction neared zero, the wavelength in the material became much larger

than the size of the entire sample, and the left-handed effects were hard to discern. Also, the frequency meant that the structure had to be very large [34]. It was for these reasons, and a desire to expand the possible application areas of metamaterials that Moser et. al. created a microfabricated rod and split-ring structure [29]. This structure operates at frequencies between 1-2.7 THz, extending the frequency range of left-handed metamaterials by three orders of magnitude, and almost into the infrared.

One possible application of the split-ring and rod metamaterial is the production of a "perfect lens," which was predicted by Pendry in 2000 [30]. In the near field of a radiating element, perfect information exists in the radiated waves. However, waves from sub-wavelength features attenuate quickly as the distance from the element increases, and are therefore called "evanescent waves." A left-handed material would amplify these evanescent waves, and therefore be able to reconstruct a perfect image of the source. This potential behavior would create sub-wavelength imaging possibilities. However, the possibility of actually achieving such behavior is under much debate. It is argued that the perfect lens relies on a lossless medium, which is impossible in reality [39]. The resolution of this debate is yet to be discovered.

Another implementation of a left-handed medium is the transmission line metamaterial. A transmission line metamaterial was created as a method to more easily interpret left-handed behavior. Also, it had significantly lower loss than the split-ring medium [12]. The transmission line metamaterial was made by building a grid of transmission line elements, each of which recreated the resonant behavior of the split-ring resonator. This structure was constructed using standard printed circuit fabrication techniques and was analyzed in two ways. One method of analysis utilized the average phase shift of a signal traveling across a unit cell to determine the bulk behavior of the material[8]. The second method for analyzing the metamaterial verified the bulk material behavior through modeling of wavefronts and S-parameters of guided wave structures with the metamaterial placed inside [3]. From these two methods, the transmission line metamaterial was determined to exhibit left-handed behavior from 1-2 GHz[8].

The transmission line metamaterial has high bandwidth over which the refractive

index is negative. Also, it is easily scalable for different frequencies, and tunable by inserting different elements into the structure. These metamaterials have already been used to make several useful advances in microwave circuits, including smaller antennas, steerable antennas, and improved branch-line couplers[26]. This thesis investigates the hypothesis that a MEMS metamaterial can utilize the advantages already achieved through metamaterials, as well as achieving these behaviors at a smaller size.

1.2.2 Antenna Applications

One application area that I will focus on in this thesis is size reduction of antennas. Specifically, I will look at patch antennas. A patch antenna is a radiating element that is constructed of two parallel conductors separated by a dielectric. The lower plate is used as the ground and is usually larger than the upper, signal plate. A directive antenna is created when the fields between the plates escape through the sides of the patch and the resulting radiation interferes. There are several methods with which one can analyze a patch antenna. One useful method is to model the patch as a thin TM-mode cavity with magnetic walls. The modes of this cavity can be determined and the effect of radiation and other losses are introduced via impedance boundary condition at the walls [5]. The fields radiated by an antenna comes from the modes of the resonator that propagate beyond the resonator.

One important parameter that is used to characterize antennas is the quality factor, Q, which can be defined as [6]:

$$Q = \frac{2\omega \text{ times the mean electric energy stored beyond the input terminals}}{\text{the power dissipated in radiation}} \tag{1.4}$$

A high value of Q can be interpreted as the inverse of the portion of the frequency band through which the antenna radiates effectively. Therefore a low Q is preferable, as it indicates that the antenna has a broad band, because the impedance varies slowly with frequency.

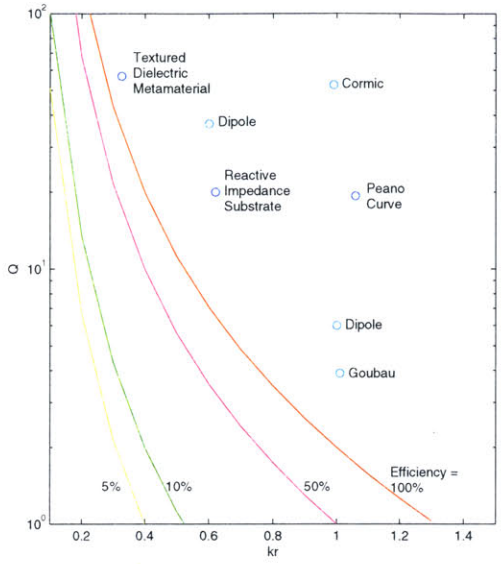

Figure 1-2: Plot of the Chu limit for various efficiencies and antennas.

As the size of an antenna is reduced if we continue to think of the structure as a resonant cavity, we see that fewer resonant modes exist. Therefore, fewer propagating modes exist for a smaller antenna and less power can be radiated. From this argument, when an antenna is made to be smaller, the Q of this antenna becomes very large. This intuitive derivation has been proven to be defined by a hard limit, called the Chu Limit:

$$Q = \frac{1 + 2(kr)^2}{(kr)^3[1 + (kr)^2]} \overset{kr \ll 1}{\approx} \frac{1}{(kr)^3} \tag{1.5}$$

Equation 1.5 represents the lowest achievable Q for any antenna that can fit within a sphere of radius r. In this equation, k is the wavevector. Figure 1-2 shows the Chu limit for various efficiency antennas. Also, data points from existing antennas are plotted. The light blue data points are standard antennas, while the dark blue are metamaterial antennas. Analysis of this plot reveals the value of efficiency in an antenna as well as the capability for metamaterial antennas to approach the optimal Chu limit.

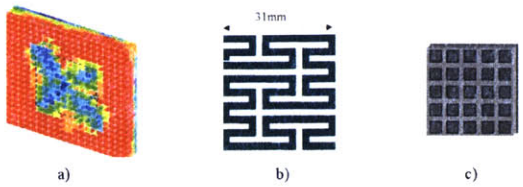

Figure 1-3: a) Textured Dielectric Metamaterial, b)Peano Curve, c)Reactive Impedance Substrate.

Metamaterial Antennas

There have been several antenna designs that have utilized metamaterials. Three of these designs are included in Figure 1-2, and indicated by the dark blue circles.

The first antenna design is the textured dielectric metamaterial antenna. In this method, the volume between the two plates of the patch antenna is broken into small cubes. The material to be placed in each cube is determined by an optimization algorithm. The resulting dielectric is therefore composed of small pieces of different dielectrics such that the effective permittivity varies with the position on the dielectric. The data shown in [23] and [24] indicate that an impressive improvement in bandwidth can be accomplished by constructing an antenna in this fashion.

A second antenna that fits under the broad topic of metamaterial antennas is an antenna produced via space-filling curves. In this design, a dipole antenna is folded in a geometric pattern in order to decrease the physical footprint of the antenna without decreasing the electrical length. However, due to this folding the antenna exhibits self-coupling and multiple resonances. One antenna, based on the Peano curve is included in Figure 1-2. The data for the point in Figure 1-2 was taken from [16]. While this design is not constructed of small unit cells, it uses a novel structure to achieve beneficial results, and therefore, I include it as a metamaterial application.

One further use of metamaterials to improve antenna performance is through the construction of a high-impedance ground plane. Also known as a perfect magnetic conductor (PMC), a high impedance surface has a reflection coefficient of $\Gamma = +1$. Therefore, if a dipole antenna were placed directly on this surface, its image current would be in phase, and the radiation performance on that side of the surface would be

greatly improved. Several types of high-impedance ground planes have been studied, including the use of space-filling curves [16].

The Reactive Impedance Substrate (RIS) is an application that is similar to the construction of a PMC, but aims to alleviate the coupling that occurs between the antenna and the ground plane in that situation. The RIS is composed of a two-dimensional metal grid pattern on top of a metal-backed, high dielectric material. Data from an antenna constructed in this manner is reported in [28] and included in Figure 1-2.

The benefits of using metamaterials in the design of antennas is clear from these examples. However, the field is still quite new, and there are many other designs to be considered, including the potential of MEMS-based designs.

1.3 MEMS

Micro-Electro-Mechanical Systems (MEMS) refers to "the integration of mechanical elements, sensors, actuators, and electronics on a common silicon substrate through microfabrication technology." [1]. The fabrication techniques for MEMS are compatible with those for integrated circuits, enabling the use of these two types of structure on a single chip. The ability to have sensors and actuators, as well as logic elements on a single chip opens exciting possibilities for completely integrated microscopic systems that can sense and control their environment.

For this research, I plan to utilize MEMS resonators to construct a metamaterial. The MEMS resonators exhibit a behavior similar to that of the rod and ring element that was used to create te first left-handed metamaterial. The difference between the MEMS and the rod and ring resonant structures is that the rod and ring element stores electromagnetic energy, while the MEMS resonator stores energy mechanically (in a physical vibration). However, by putting electrostatically-actuated MEMS resonators in a periodic array similar to the one used for the rod and ring structure, they may exhibit a similarly beneficial electromagnetic behavior. The MEMS resonators are explored more thoroughly in Chapter 2.

MEMS resonators are good candidates for the creation of a metamaterial for many reasons. One powerful reason is a great amount of flexibility in resonant frequency. The dimensions of the resonator, which are easily adjustable, dictate its behavior in a predictable manner. This should make a medium created with the MEMS resonators very versatile. Typical measured resonant frequencies of the MEMS resonators range from 100 MHz to 2 GHz. The small size of the resonator is another benefit. Many of the resonators can be combined in an area smaller than a wavelength, creating the possibility for complex metamaterial behaviors and smaller devices. Finally, the ease of integration with existing circuit fabrication processes and circuit structures will make a MEMS-based metamaterial more practical to include in most applications. With all these potential benefits, a metamaterial constructed with MEMS resonators is a worthy purpose.

Chapter 2

MEMS Resonators

A Micro-Electro-Mechanical System (MEMS) device that exhibits some sort of mechanically resonant behavior is called a MEMS resonator. The most common type of MEMS resonator is the cantilever, which is simply a bar that is secured at one end and has a natural frequency of oscillation that is determined by its dimensions and material parameters. The cantilever can be driven electrostatically with a conducting pad that creates a potential between itself and the cantilever, creating a force. MEMS resonators are already an important part of devices including microgyroscopes, microvibrators, microengines, and RF systems [27].

I plan to use MEMS to create a metamaterial because the small size, high Q, and ease of integration with circuit fabrication processes that they offer. In this chapter, we will compare two types of electrostatically-driven MEMS resonators and find the resonator that is most fitting for potential use in a metamaterial. The two types are the paddle resonator and the piezoelectric resonator.

2.1 Paddle Resonator

A paddle resonator consists of a rectangular solid (the paddle) suspended over an open trench by two thin supporting rods that bisect opposite sides of the paddle. Figure 2-1 is a picture of a paddle resonator. When driven by a potential from a conducting pad underneath one side of the paddle, the structure will vibrate. There

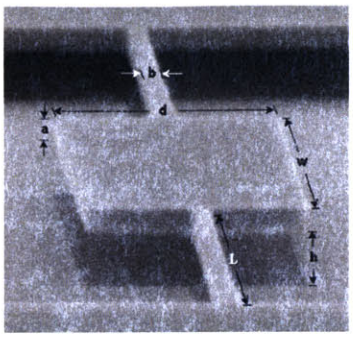

Figure 2-1: A MEMS paddle resonator with the dimensions labeled. From [9]

are several modes of vibration for the paddle, including shifting up and down, left and right, and twisting in a "see-saw" motion. This last mode is the torsional mode, and it is the one that we will focus on, as it occurs at the highest frequencies. We are analyzing the paddle resonator because it is a popular, well-documented design and its torsional mode operates at frequencies nearing the band in which we are interested.

To analyze this resonator, we place it in series with a coplanar transmission line (CPW) such that the middle, signal, line runs below the paddle, exciting the resonance electrostatically. The signal line is broken under the resonator, forcing the signal through the resonator. Figure 2-2 shows this structure. We are then able to model this structure as a circuit, using standard electromagnetic techniques to determine the capacitance and inductance of pieces of the system, based on their geometry and material parameters. This analysis is similar to that performed on other types of metamaterial [18] [8].

The first step in our analysis of the paddle resonator is to analyze the circuit without any resonant behavior. The goal of this step is to determine if the off-resonance behavior of the resonator is desirable for our applications. The next stem in the analysis is to determine how the mechanical resonance changes the behavior of the system. Finally, we determine the performance of the system by calculating the attenuation of a signal that is passed through the resonator.

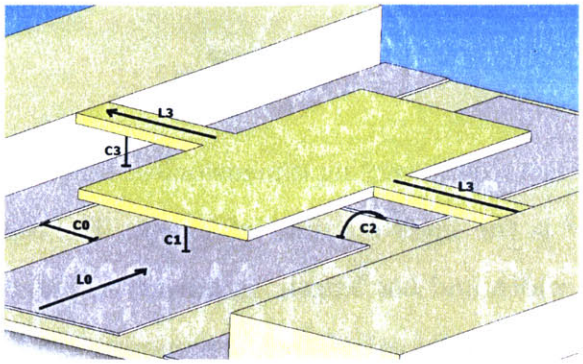

Figure 2-2: Three-dimensional model of the paddle resonator with lumped circuit elements labeled.

2.1.1 Broadband Analysis

To analyze the resonator we need to be able to describe its behavior numerically. First, we determine the natural frequency of oscillation and signal attenuation (loss) as a function of geometry. The circuit elements that are produced by the geometry are labeled in Figure 2-2 and the equivalent circuit is shown in Figure 2-3. Using this model, we determine the optimal dimensions of the resonator that will oscillate at a desired frequency with minimum loss.

Natural Frequency

To utilize the resonator, we must be working at and around its natural frequency. Therefore, in my analysis of these paddle resonators, I needed to be able to determine the natural frequency of a resonator from its dimensions and other material parameters.

The natural frequency of the torsional mode of the paddle resonator is given by Equation 2.1, taken from [9]:

$$f_0 = \frac{1}{2\pi}\sqrt{\frac{\kappa}{I}} \tag{2.1}$$

Where κ is a torsional constant and I is the moment of inertia about the center axis of the paddle along the line of its tethers. The torsional constant can be predicted with the equation from [10]:

$$\kappa = 2\beta\left(\frac{a}{b}\right)\frac{ab^3}{L}G \tag{2.2}$$

In this equation, β is a slowly varying dimensionless function of the ratio b/a, and $G_{si} = 6.7 \times 10^{10} Nm^{-2}$ is the shear modulus of silicon. The dimensions a, b, and L, are the thickness, bar width and bar length, as labeled in Figure 2-1.

The moment of inertia can be calculated by summing the inertia of pieces of the resonator about the same axis. I chose to break the paddle resonator into three pieces: the paddle, and the two tethers. Then I calculated the moment of inertia.

$$\begin{aligned} I_{resonator} &= I_{paddle} + 2I_{tether} \\ &= \frac{m_{paddle}}{12}(a^2 + d^2) + 2\frac{m_{tether}}{12}(a^2 + b^2) \\ &= \frac{a\rho}{12}(a^2dw + d^3w + 2a^2bL + 2b^3L) \end{aligned} \tag{2.3}$$

The mass of each piece was calculated by multiplying the volume of that piece by ρ, the density. In silicon, $\rho = 2330$ kg m^{-3}. Inserting the value for the inertia from Equation 2.3 into Equation 2.1, the natural frequency of the torsional mode of a paddle resonator is:

$$f_0 = \sqrt{\frac{3}{\pi^2}\frac{\kappa}{\rho a(wd^3 + wd^2a + 2a^2bL + 2b^3L)}} \tag{2.4}$$

In [9] the denominator in the equation for the natural frequency only contains the first term (ρawd^3). The other terms did not make a difference in their measured results. Therefore, I also dropped these terms to simplify my calculations, and to adhere to physically realized models.

Analysis of Loss Through Resonator Structure

Creating a circuit from the elements labeled in Figure 2-2, I created the circuit model shown in Figure 2-3. This circuit is the equivalent circuit for a broadband analysis of the paddle resonator. In this context, broadband refers to the off-resonance response.

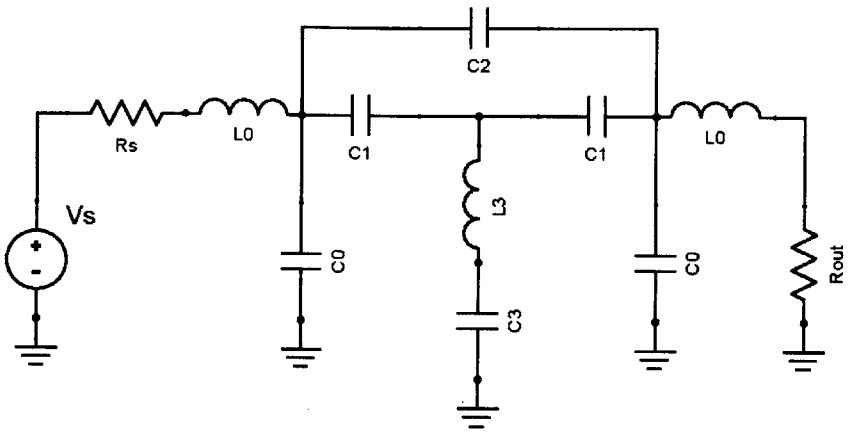

Figure 2-3: Broadband equivalent circuit model of the paddle resonator

In this condition, the system behaves like the circuit in Figure 2-3 across all frequencies of excitation from V_s. This broadband analysis was performed to provide a baseline measure of the signal through the paddle.

$$R_s = R_{out} = 50\Omega$$

$$C_1 = \frac{\epsilon\left(\frac{d-b}{2}\right)w}{h}, \qquad L_3 = \frac{\mu L h}{b}, \qquad C_3 = \frac{\epsilon L b}{h} \tag{2.5}$$

L_0, C_0, and C_2 are determined by the coplanar waveguide equations from Section 3.7 of this thesis.

The signal attenuation through this system is determined by comparing the ratio of the voltage across the input resistor, R_s, to the voltage across the output resistor, R_{out}. These voltages are obtained through straightforward circuit analysis.

When performing the circuit analysis, I assumed the metal was a perfect conductor and ignored losses through fringing fields. Additionally, I ignored the capacitor C2, as its effects are almost purely due to fringing fields, and its size and effects are negligible when compared to the other circuit elements. With these assumptions, the ratio of the output voltage to the input voltage is:

$$\frac{V_{out}}{V_s} = \frac{R_{out}}{Z_{in}} \tag{2.6}$$

Where Z_{in} is the impedance of the system from the source node. This impedance is calculated using the following equations;

$$Z_{in} = j\omega L0 + Z_2 \tag{2.7}$$

$$Z_2 = \frac{1}{j\omega C0 + \left(\frac{1}{\frac{1}{j\omega C1} + Z_3}\right)}$$

$$Z_3 = \frac{1}{\left(\frac{1}{j\omega L3 + \frac{1}{j\omega C3}}\right) + \left(\frac{1}{\frac{1}{j\omega C1} + Z_4}\right)}$$

And finally:

$$Z_4 = \frac{1}{j\omega C0 + \frac{1}{(j\omega L0 + R_{out})}}$$

Substituting the equations for the circuit parameters as a function of physical dimensions (Equations 2.5) into Equation 2.6 and its subsequent definitions of impedances, we obtain a mathematical formula for the signal that is passed through the system as a function of the physical size. Additionally, from Equation 2.4, we know the frequency of operation at which we should operate. Therefore, we have an entire mathematical description of the interesting parts of the system (ignoring the physical resonance) as a function of physical dimensions.

Using these equations that describe the electrical behavior as a function of physical size, we can determine the optimal size of a paddle resonator to achieve the desired electrical behavior. In order to find the optimal values for each dimension, I used a random-restart hill climbing algorithm [19], [17]. The algorithm adjusts the dimensions of the resonator model and calculates the loss and natural frequency for that size. From these results, a change is made to the dimensions to step towards an optimum point where the signal loss is at a minimum and the natural frequency is near the desired frequency of operation. When the algorithm converges, it saves the data, and then begins again with random starting values. This is done to increase the

chances that we will reach a global optimum, instead of becoming trapped at local optima. In this manner, I find the dimensions of a resonator that would function with the least loss near a desired frequency.

Looking at Equations 2.5, some conclusions about the optimal dimensions can be drawn before running any optimization. First, the maximum value for a is desirable because a large a leads to a higher natural frequency (which we need because we want to work in a frequency range that is higher than usually used for these resonators), also the large value of a has no adverse effects to the electrical behavior of the circuit. Another preliminary optimization choice is realized by noticing that a small h will increase C1, and result in less loss. So h should be at the minimum value possible. However, while it is obvious that increasing d and w will increase C1, and result in less loss, these changes will also decrease the (already low) natural frequency of the oscillator (via an increased paddle mass and an increased moment of inertia). Similarly, while decreasing b will decrease the loss capacitance C3, it will increase the inductance L3, so without the values of L3 and C3 the overall effect on the system is unclear. These ambiguities are the reason for using the optimization algorithm. The maximum and minimum constraints for each dimension are shown in Table 2.1.

Note that a is fixed at 100μm. This value is the maximum that a can reasonably obtain with conventional fabrication methods. Conversely, although h should be at a minimum, it was included in the optimization because a very small h could cause trouble with the oscillatory motion of the resonator. While we were not considering this motion in the current electrical analysis, it is an important factor to consider and therefore was included to determine if there were any near optimal configurations that did not include the minimum value of h.

An additional constraint in the optimization, denoted by the stars (*) in Table 2.1, is that the values of W and L are related such that $2L+W \geq 150\mu$m. This constraint is used so the resonator structure is sure to span the transmission line which has a minimum total width of 150μm.

The optimization analysis was carried out for frequencies of 100MHz, 500MHz, and 1GHz. The resulting optima are shown in Table 2.2.

Table 2.1: Constraints used for paddle resonator optimization

Dimension	**Minimum**	**Maximum**
a	100μm	100μm
b	1nm	250μm
d	1nm	250μm
h	1nm	100μm
L	1μm*	250μm
W	1μm*	250μm
Frequency	$f_0 - 10$MHz	$f_0 + 10$MHz

Table 2.2: Optimum dimensions of paddle resonators for three target frequencies.

Target Freq	f_0	**a**	**b**	**d**	**h**	**L**	**W**	$\frac{V_{out}}{V_{in}}$**(dB)**
100MHz	91.3MHz	100μm	1.31μm	2.56μm	1nm	27μm	96μm	-74
500MHz	491 MHz	100μm	110nm	116nm	1nm	27μm	96μm	-102
1GHz	.995 GHz	100μm	30nm	40 nm	1nm	27μm	96μm	-131

Judging from the results in Table 2.2, without the mechanical resonance, a paddle structure does not perform well. The best signal strength, at 100MHz, is -74 dB. This means that when 1 Volt is across the input terminals, 0.2 mV can be detected at the output. While this behavior is not terrible, it is also not easy to achieve; obtaining a thickness of 100μm as well as a gap size of 1nm would be incredibly expensive, if possible at all. Additionally, when we work in higher frequency ranges, the paddles with dimensions in the tens of nano-meters would be incredibly difficult to fabricate while maintaining the large aspect ratio of 100μm. Because the goal of introducing MEMS in this thesis is to create an effective, easy, cheap solution, paddle structures do not appear to fulfill the requirements. The money required could be spent on much more effective systems.

However, in the next section, we add the mechanical resonance to the model of the paddle. This resonance could potentially decrease the impedance enough such that the paddle resonator becomes a viable option for the construction of a metamaterial.

2.1.2 Resonance analysis

In the previous section, I modeled the gap between the paddle of a paddle resonator and a transmission line that was driving it as a constant-valued capacitor. The equation that determined the current flowing through the capacitor was $I_C = C\frac{dV}{dt}$. If we want to consider the mechanical resonance of the device, this equation no longer captures the entire behavior of this structure.

To build the more complete model, we must consider how the motion of the paddle changes the electrical characteristics of the system. To do this, we first consider the current passing through the gap from the transmission line to the paddle. The definition of current is the flow of charge. The charge on a capacitor is defined as the voltage across the capacitor times its capacitor. Taking the derivative of this definition of charge to find the complete equation for the current through the capacitor we get:

$$I = \frac{dQ}{dt} = V\frac{dC}{dt} + C\frac{dV}{dt} \tag{2.8}$$

This equation can be thought of as a mechanical device in parallel with an electrical one. The currents through the two elements add to produce the total current. The second term of the rightmost portion of Equation 2.8 is the standard electrical definition of current through a capacitor. This represents the electrical component of our parallel system. The other term in Equation 2.8 indicates that the current is also related to the change of capacitance with respect to time. This value changes in our paddle resonator; as the paddle oscillates, the paddle moves closer and further from the driving transmission line, increasing and decreasing the capacitance, and changing the impedance by more than the change in capacitance alone. Therefore, if this component of Equation 2.8 is large, the paddle resonator may pass enough current at resonance to act as desired.

The change in capacitance of the gap between the transmission line and the paddle is related directly to the velocity of the resonator. To find this velocity, we use the standard equation for the harmonic motion of a resonator:

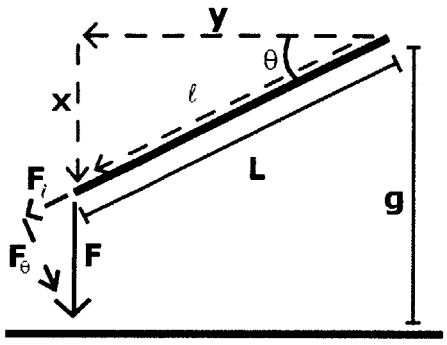

Figure 2-4: A force diagram for one side of the paddle resonator. (Restoring force is not included)

$$I\ddot{\theta} + \frac{I\omega_0}{Q}\dot{\theta} + \kappa\theta = \tau(\omega t, \theta) \tag{2.9}$$

In this equation θ is the angular displacement of the resonator, as shown in Figure 2.1.2. Its first and second derivatives are indicated by $\dot{\theta}$ and $\ddot{\theta}$. The variables I and κ are the moment of inertia and torsional constant, respectively. Equations for these parameters were defined in Equations 2.3 and 2.2 earlier in this chapter. The natural (angular) frequency, ω_0, can be obtained easily from the natural frequency obtained from Equation 2.4. The quality factor of the resonator, Q, is a product of material properties and resonator construction. The parameter g is the distance between the cantilever and the transmission line when θ is zero. Finally, τ indicates the driving torque on the resonator from the transmission line. Note that this is a function of the voltage on the transmission line (which is a function of ωt as well as the angular displacement, θ).

Before continuing, one note must be made; the rest of the analysis in this section focuses on only one half of the paddle resonator. The other half is assumed to be directly connected to the output and does not contribute to the resonant or electrical behavior. This simplification is justified because the goal of this analysis is to determine if the mechanical resonance is large enough to produce any measurable difference in the impedance of our system. In the analysis of one side of the paddle resonator, the resonant behavior is similar to that of the double-sided paddle and the

electrical behavior is much improved. The resonant behavior is similar because the resonator obeys the same resonance equation, with just a changed moment of inertia. The electrical behavior is much improved because the capacitance between the resonator and the driving and sensing transmission lines was the source of the most loss in the previous section. By bypassing the second half of the paddle resonator, we are removing half of that loss. Therefore, the resulting analysis using only one half of the paddle resonator is a viable option to determine if the mechanical resonance of this type of resonator produces enough change in the impedance to make the device a candidate for the use in a metamaterial. With that stated, we continue our analysis by finding the torque on the bar.

To find an expression for the torque, one first calculates the torque due to one small piece of the bar as a function of theta and its length along the bar. Then the force is summed for all the pieces along the bar to get the total torque. This process is shown in Appendix A.2. The torque that is obtained from the analysis is:

$$\tau = \frac{V^2 \epsilon_0 w \cos\theta}{2\sin^2\theta}\left(\frac{L\sin\theta}{g - L\sin\theta} - \ln\frac{g}{g - L\sin\theta}\right) \tag{2.10}$$

To simplify the analysis we can take the Taylor expansion of τ to obtain:

$$\tau \approx \frac{1}{4}\frac{w\epsilon_0 V^2 L^2}{g^2} + \frac{1}{3}\frac{w\epsilon_0 V^2 L^3}{g^3}\theta + \frac{1}{8}\frac{w\epsilon_0 V^2 L^2}{g^2}\left(\frac{3L^2}{g^2} - 1\right)\theta^2 + \cdots \tag{2.11}$$

Where the $\cdots$ indicate the higher order terms that we can ignore. Note that for the Taylor expansion to be valid, the ratio $\frac{L}{g} \gg \sin\theta$. Because this ratio of the length of the paddle to the gap is much greater than one for all time in our optimal configurations (shown in Table 2.2), this requirement is always satisfied, and it is therefore safe to use the Taylor expansion result in the following analysis.

Note that the torque is proportional to the square of the electrostatic driving voltage. If we define our input voltage as a DC bias and an AC signal driving voltage:

$$V = V_{dc} + V_{ac}\sin\omega$$

Then the torque is proportional to the square of this voltage and has second-order harmonics:

$$\begin{aligned}\tau \propto V^2 &= V_{dc}^2 + 2V_{dc}V_{ac}\sin\omega + (V_{ac}\sin\omega)^2 \\ &= V_{dc}^2 + 2V_{dc}V_{ac}\sin\omega + V_{ac}^2\left(\frac{1}{2} - \frac{\cos 2\omega}{2}\right) \\ &= \left(V_{dc}^2 + \frac{V_{ac}^2}{2}\right) + 2V_{dc}V_{ac}\sin\omega - \frac{V_{ac}^2}{2}\cos 2\omega \end{aligned} \tag{2.12}$$

The second order harmonic brought about by the $\sin\omega^2$ term is undesirable. This value can be neglected if $V_{dc} \gg V_{ac}$, which linearizes Equation 2.12. We now can substitute the equation for torque into the equation of motion of the resonator (Equation 2.9) and solve for $\dot{\theta}$, the velocity of the cantilever. The velocity of the cantilever can then be used to determine the velocity of the change in capacitance, which in turn will be used to determine the current flowing through our system.

Another important feature of Equation 2.11 is that it includes a term that is independent of the angle θ. This indicates a constant torque that acts on the bar [1]. This torque is important in our analysis because it creates a constant angle of displacement, θ_{dc}, that we must consider to ensure that the total angle of displacement of the bar is not so large that the bar ever contacts the driving line.

To solve for θ we calculate the transfer function for the resonant behavior of the bar. We get the transfer from Equations 2.9 and 2.11. In this equation $s = i\omega$:

$$Is^2\theta + \frac{I\omega_0}{Q}s\theta + \kappa\theta = \frac{1}{4}\frac{w\epsilon_0 V^2 L^2}{g^2} + \frac{1}{3}\frac{w\epsilon_0 V^2 L^3}{g^3}\theta + \cdots \tag{2.13}$$

For the frequency-independent component of the displacment angle, θ_{dc}, the transfer function consists of all the frequency independent parts of Equation 2.13 (the parts without an s). Also, we only consider the constant torque and the frequency-independent terms of the voltage. Solving for θ_{dc}, we obtain:

[1] This constant torque is from the force of gravity on the one-sided paddle. In the case of the two-sided paddle, this term is caused by asymmetries in the sides of the paddle[4].

$$\theta_{dc} = \frac{\left(V_{dc}^2 + \frac{V_{ac}^2}{2}\right) w\epsilon_0 L^2}{4\kappa g^2}$$

Using the optimal values for a resonator at 100MHz as shown in Table 2.2, we obtain $\theta_{dc} = 1.174 \cdot 10^{-6}$ degrees.

To calculate the frequency-dependent portion of the angular displacement, θ_{ac}, we consider the all terms of Equation 2.13. However, when substituting in for V^2 from Equation 2.12, we utilize the frequency-independent term of V in the angle-independent portion of τ and the frequency-dependent term in the rest. This is because, in this frequency analysis, the the constant portion of the torque cannot be dependent on frequency. After solving for θ_{ac}, we obtain:

$$\theta_{ac} = \frac{w\epsilon_0 L^2 (2V_{dc}V_{ac})}{4g^2\left(Is^2 + \frac{I\omega_0}{Q}s + \kappa - \frac{w\epsilon_0 d^3\left(V_{dc}^2 - \frac{V_{ac}^2}{2}\right)}{g^3}\right)} \tag{2.14}$$

The velocity of the bar is $\dot{\theta} = s\theta$. Now, to find the change in capacitance that will cause the current that we are interested in, calculate the change in capacitance due to the change in θ of a small piece of the bar of length dl and integrate along the length of the bar.

$$\frac{dC}{d\theta} = \int_0^L \frac{\epsilon_0 wl\cos\theta}{(g - l\sin\theta)^2} dl \tag{2.15}$$

As mentioned earlier, the current due to the mechanical resonance can be thought of as an independent device in parallel with the electrical device that we analyzed in Section 2.1.1. The impedance of this device is defined as the voltage across it divided as the current through it. Looking at Equation 2.8, we see that the mechanical impedance is therefore:

$$Z_{mech} = \frac{V}{I_{mech}} = \frac{1}{\left(\frac{dC}{dt}\right)}$$

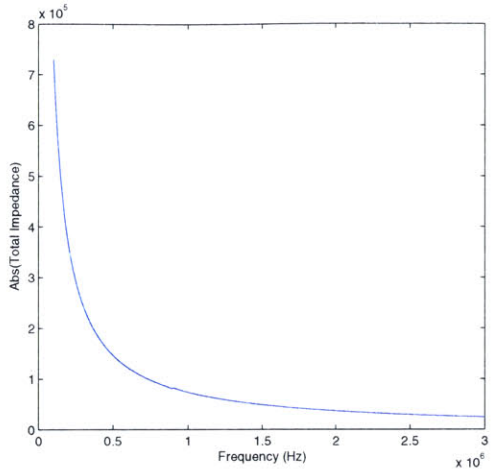

Figure 2-5: Impedance of the paddle resonator. Values are from Table 2.2 and $Q = 5000$.

If we combine this impedance in parallel with the impedance of the electrical component of the system from Equation 2.7, we find the impedance of the entire system. The results from this combination are shown in Figures 2-5 and 2-6. Note in these graphs, the dimensions used are those discovered to be optimum for the 100MHz resonator in Table 2.2 and $Q = 5000$. Figure 2-6 is an enlarged view of the resonant portion of 2-5.

2.1.3 Evaluation

Using the impedance of the system that includes the mechanical resonant behavior obtained in the previous section, we are able to perform the loss analysis from Section 2.1.1 again, but this time including the mechanical behavior with the hopes that it will cause a large change in the signal that is passed through the system. We use Equation 2.6, but in this case Z_{in} is the parallel combination of the electrical and mechanical impedances that was shown in Figures 2-5 and 2-6.

The resulting ratio of output to input voltages (in dB) is shown in Figures 2-7 and 2-8. Figure 2-8 is an enlarged view of the resonant portion of 2-7.

These graphs show that, while the mechanical resonance does change the magnitude of the signal that is passed through the system, the change is not enough to

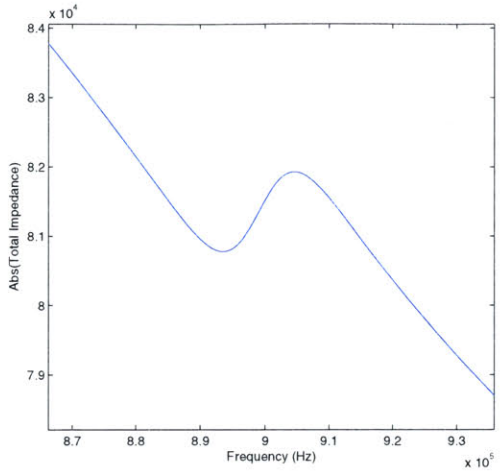

Figure 2-6: Closer view of resonance of impedance of the paddle resonator.

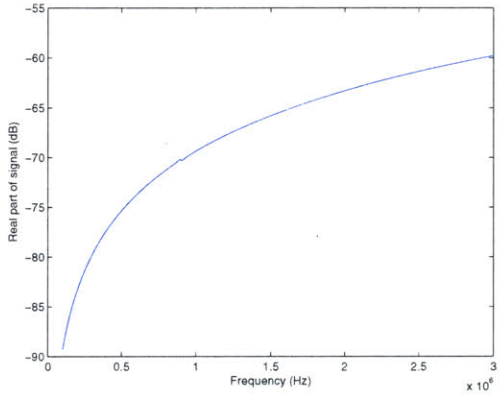

Figure 2-7: Signal through the paddle resonator. (dB)

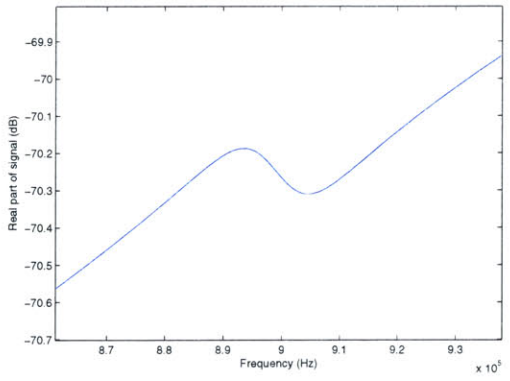

Figure 2-8: Closer view of resonance of signal passed through paddle resonator.

bring the signal into any usable region.

Next we will evaluate the Draper piezoelectric resonator in the same manner, to compare its performance to that of the paddle resonator.

2.2 Draper Resonator

The piezoelectric MEMS resonator developed by the Charles Stark Draper Laboratory boasts the characteristics that are desired in a resonator to be used in a metamaterial. It has a simple coplanar design, operates in the desired frequency region, and has a very small footprint. The resonator consists of a piezoelectric substrate (Aluminum Nitride) sandwiched between two electrodes, suspended above a well to allow for vibration. An electric potential across the electrodes of the resonator will induce a mechanical strain in the piezoelectric AlN. An AC voltage can be chosen to match the mechanical resonance of the device. At this frequency the MEMS device exhibits large amplitude vibration and passes current with low impedance.

The piezoelectric equations of state relate the electric field and charge polarization to the mechanical parameters of the resonator. Analysis of these equations can produce a relationship between the voltage across the resonator to the current through it [21]. The existence of this relation indicates that the MEMS resonator can be represented as a collection of circuit elements, as was the split-ring-resonator.

2.2.1 Fabrication and Measurement

The resonator consists of a piezoelectric substrate sandwiched between two conducting bars. In the measured device, the metal bars were constructed of 300 $\AA$ of Chromium over 1500 $\AA$ of Platinum. The bar was 4 um wide by 41 um long. The device was fabricated by James Hsiao at the Charles Stark Draper Laboratory. Figure 2-9 shows the S21 parameters that were obtained from measurements of this device.

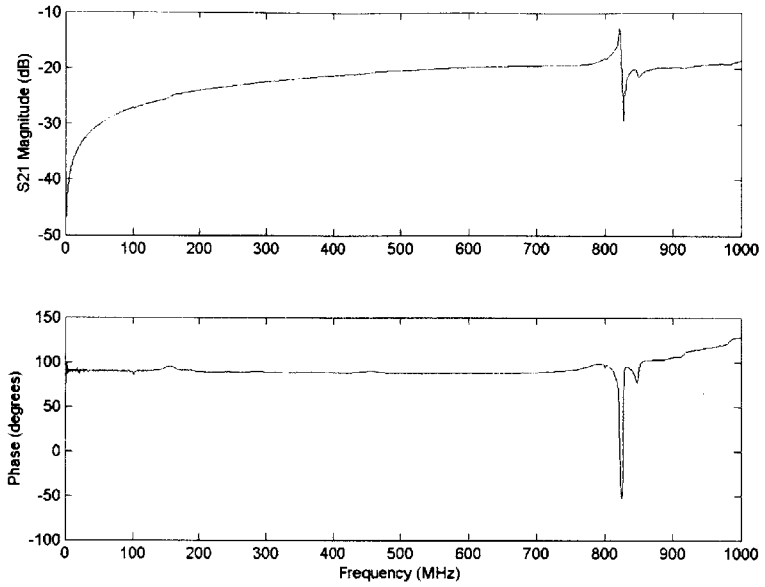

Figure 2-9: Measured S21 values of the piezoelectric resonator.

2.2.2 Parameter Extraction

The Butterworth Van-Dyke (BVD) model is a common way to simplify the transcendental functions that completely characterize resonators. The circuit used for the BVD model is shown in Figure 2-10. This circuit accurately models a single resonance and models regions not near this resonance as a capacitance.

Through analysis of the constitutive equations of the resonator, values for the BVD circuit elements can be produced. This equivalent circuit can then be used for

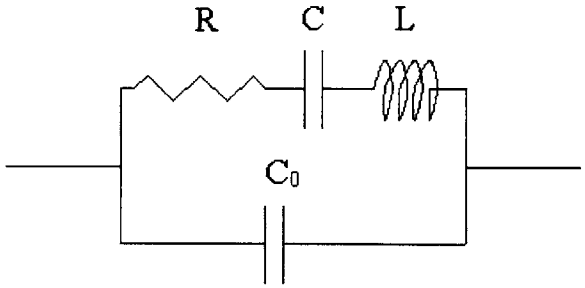

Figure 2-10: BVD model of a resonant structure.

Table 2.3: Values of BVD model of measured piezoelectric resonator data.

Dimension	C_0	C	L	R
Value	24.1627 fF	0.308356 fF	121.572 μH	1967.64 Ω

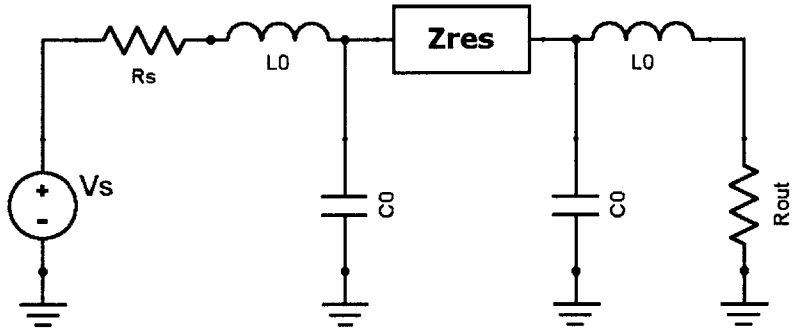

Figure 2-11: Equivalent circuit model of the piezoelectric resonator in series with the transmission line.

analysis, modeling, and design of structures using the resonator.

A curve-fitting algorithm was used on the data from the measured devices, determining the extracted circuit parameters for the piezoelectric resonator. The curve fitting was performed by James Kang at the Charles Stark Draper Laboratory. The parameters that were obtained are shown in Table 2.3.

2.2.3 Resonance Analysis

With the equivalent circuit parameters obtained from fitting the BVD model to the measured data, I was able to perform the same loss analysis on the piezoelectric resonator as I did on the paddle resonator. The circuit obtained by placing the resonator in series with the transmission line is shown in Figure 2-11.

By performing a standard circuit analysis, I obtained the impedance shown in Figure 2-12 and the signal attenuation shown in Figure 2-13.

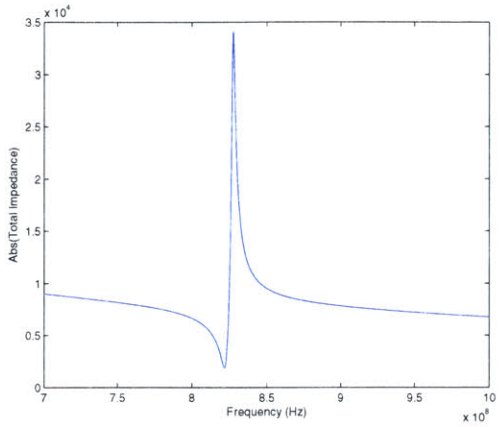

Figure 2-12: Impedance of the piezoelectric resonator.

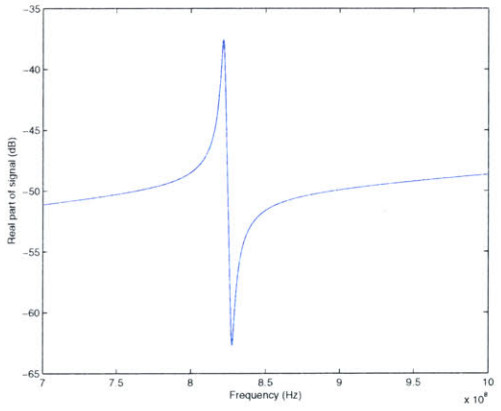

Figure 2-13: The signal passed through the piezoelectric resonator.

2.3 Comparison

To compare the two resonators for use in a metamaterial, we simply compare Figures 2-7 and 2-13. These graphs demonstrate the portion of a signal that will pass through a single element of the resonators when driven and loaded with matched 50 Ohm impedances. The paddle resonator, shown in Figure 2-7 has a huge amount of loss throughout the entire frequency sweep. Also, the resonant behavior is barely noticeable. The diminutive magnitude of the resonant peak is undesirable for two reasons: First, the small magnitude means that the signal strength never rises to a usable level. Therefore, any system using even one of these resonators in the manner that we are planning cannot possibly get a usable signal at its output. The second drawback of the small resonant peak is that the behavior of the metamaterial is based on that resonance. If the peak is small, the left-handed behavior that we are looking for may be difficult to discern.

The piezoelectric resonator, shown in Figure 2-13, not only has a much better signal strength throughout the entire frequency sweep, it also has a much larger resonance. Therefore, a useful signal could be passed through this system, and if left-handed behavior occurs, it should be noticeable. Additionally, the large resonance may be able to provide us with a greater range of resulting metamaterial values that we can potentially access through the use of these resonators.

Therefore, if we were to construct a MEMS-based metamaterial, the Draper piezoelectric resonator would be the preferred resonator to use.

Chapter 3

Dispersion Analysis

One valuable characteristic of left-handed metamaterials, as mentioned in the introductory chapter, is that the phase velocity of a wave traveling through the material has a sign opposite of the group velocity for that wave. If the phase velocity, which is normally positive, can be negative, then it conceivably can reach many of the values in between. Therefore, some exciting applications for left-handed metamaterials as well as metamaterials in general would involve utilizing this unusual phase-shifting behavior. Two example metamaterial applications explore this idea in phase shifters and antennas.

Phase-shifting circuit elements are an important aspect of many RF circuits, specifically in antenna feed networks. A phase shift is usually accomplished by simply having the signal run through the appropriate length of transmission line. This method of phase shifting uses a lot of space and can create spurious fields that can interfere with other parts of the circuit. A metamaterial could potentially be used to shift the phase of a signal in a much more compact component.

The dimensions of an antenna are usually determined by the frequency at which the antenna is designed to function. An ideal antenna would be some multiple (or half multiple) of a wavelength so the structure can support a standing wave. Antennas usually do not satisfy this constraint because the designers either needed to the antenna to be smaller than a wavelength, or the antenna was simply not allotted the required volume. When an antenna is not at its ideal dimensions, reflections from

the edges of the antenna interfere with the standing wave, and the antenna loses efficiency. If it were possible to use a metamaterial to produce the correct phase shift (a multiple or half multiple of π) across the antenna, it would be possible to fit more efficient antennas in smaller spaces as well as tune the antenna to operate efficiently in the size that is allotted for it.

Because the phase shift through a metamaterial can produce such interesting and useful applications, we must look into the dispersion relation of the potential metamaterial. The dispersion relation is an analysis of the association between the frequency of a wave and the phase shift through a given size of a media. By looking at this relationship, we can determine if a given metamaterial demonstrates the behavior that will be beneficial for phase-shifting applications.

3.1 Equivalent Circuit Model

As with the loss analysis in Chapter 2, in order to explore the behavior of this system, we must first make a model. The model of the resonator used in this chapter is the same as the BVD model used for the piezoelectric resonator in Chapter 2. This resonator is then placed in various architectures to be analyzed. In most of the analyses in this section, the resonators are assumed to be in an infinite periodic array. The system shown is one unit cell that is repeated ad infinitum. In this way, there are no reflections between unit cells.

3.2 Dispersion Analysis Methods

Another important step in the study of a metamaterial is validating the accuracy of the chosen analysis methods. There are several methods for finding the phase shift through a unit cell of the material. While all these methods should be equivalent, there are slight differences in the assumptions that they make about the material. Because we are not dealing with a "normal" material, these assumptions may not be valid in our work. It is therefore important to discover these assumptions and

determine if the method is still a useful way to analyze our metamaterial.

In order to evaluate these models, I performed the dispersion analysis on several structures. The structures started out as a single transmission line and slowly approached the proposed metamaterial by adding circuit elements to the unit cell. Each of the intermediate steps are simple enough, and it should therefore be possible to determine if any of the analysis methods produce incorrect results at any step. If, after going through all of the steps, I am confident in the accuracy of the method, I can use it to analyze other, unknown structures.

3.2.1 ABCD Matrix

The transmission, or ABCD matrix, is a useful method for characterizing a microwave network. For a network with two ports (1 and 2) where the voltage and current at port n are V_n and I_n, the transmission matrix elements are defined as:

$$\begin{aligned} V_1 &= AV_2 + BI_2 \\ I_1 &= CV_2 + DI_2 \end{aligned} \tag{3.1}$$

or in matrix form:

$$\begin{bmatrix} V_1 \\ I_1 \end{bmatrix} = \begin{bmatrix} A & B \\ C & D \end{bmatrix} \begin{bmatrix} V_2 \\ I_2 \end{bmatrix}$$

The ABCD matrix is useful because in this form, the matrix representing the cascade of multiple networks is simply the product of their matrices. Further information about the ABCD matrix can be found in [33]. Also in [33], there is a definition for the phase shift across a unit cell in a periodic array of elements defined by an ABCD matrix. That relation is:

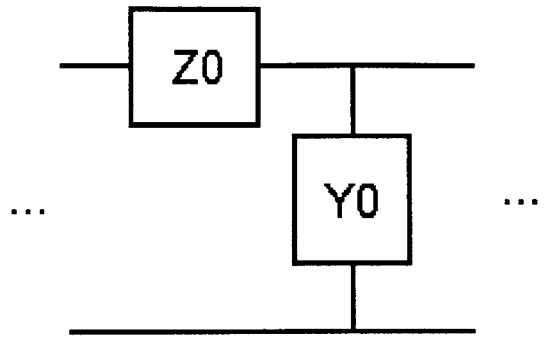

Figure 3-1: Unit cell of general lumped element line.

$$\cosh \gamma d = \frac{A + D}{2} \tag{3.2}$$

Where A and D are the parameters from the ABCD matrix and gamma is the complex propagation factor, $\gamma = \alpha + j\beta$ such that:

$$\begin{aligned} V(z) &= V(0)e^{-\gamma z} \\ I(z) &= I(0)e^{-\gamma z} \end{aligned}$$

Note that β, the imaginary part of γ, is the phase shift and the real part, α, is the loss tangent.

3.2.2 Impedance and Admittance

The dispersion relation for an infinite, periodic line of general lumped elements is given in [25]. A single element of this line is shown in Figure 3-1.

If Z_0 and Y_0 are functions of frequency, the dispersion relation of this structure will indicate the relationship between the frequency and wavelength of a signal traveling across it. The dispersion relation of a repeating structure made from these unit cells can be represented by Equation 3.3. In this equation, θ is the phase shift across the unit cell. In other words, $\theta = kl$, where k is the wavenumber and l is the length of

the unit cell.

Therefore, if we were to compare this method to the previous method (using the ABCD matrix), we see that $\theta = -jl\gamma$, where l is the length of a unit cell.

$$\sin^2 \frac{\theta}{2} = -\frac{1}{4} Z_0 Y_0 \tag{3.3}$$

3.2.3 Full-Wave Simulation

Additionally, two full-wave simulation software tools were used. Full-wave simulators are computer programs that use Maxwell's equations to simulate electromagnetic wave propagation subject to boundary conditions imposed by physical structures. These tools allow the user to construct a model of the physical structure, including sources and detectors of EM phenomena. Then the simulation can be used to determine the behavior of EM waves in an around this structure. The two tools used were Sonnet Lite and Ansoft High Frequency Structure Simulator (HFSS).

3.3 Dispersion Analysis of Simple Structures

I performed the dispersion analysis on two simple structures to build confidence in the accuracy of the two methods. The two simple structures were a transmission line and a transmission line with a capacitor in series.

3.3.1 Transmission Line

The first structure is a simple transmission line. This consists of two parallel conducting plates separated by a dielectric material. The transmission line can be modeled by its characteristic values of line inductance and shunt capacitance, L_0 and C_0.

In the impedance analysis method, the line inductance and shunt capacitance map directly to the impedance and admittance.

$$Z_0 = L_0$$

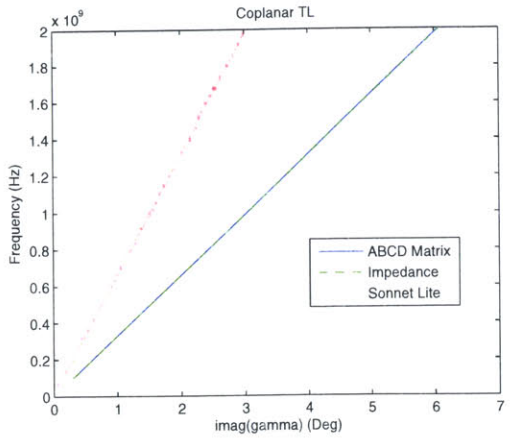

Figure 3-2: Simulated value for the phase shift across a transmission line using numerical and full-wave simulations.

$$Y_0 = C_0$$

The ABCD matrix has a standard form for a transmission line:

$$\begin{bmatrix} A & B \\ C & D \end{bmatrix} = \begin{bmatrix} \cos\beta l & jZ_0 \sin\beta l \\ jY_0 \sin\beta l & \cos\beta l \end{bmatrix} \tag{3.4}$$

Here βl is the imaginary part of the propagation factor times the unit length of a cell. Because we are assuming a lossless transmission line, the propagation factor is purely imaginary and the product $\beta l = \omega\sqrt{L_0 C_0}$. The simulation results are plotted in Figure 3-2.

The simulations behave exactly as expected. As the frequency increases, the phase shift across a unit cell increases. The slope of this line is the speed of light in the transmission line. Furthermore, the impedance and the ABCD matrix methods return the exact same values. The full-wave simulation was slightly different, but that is to be expected, as this simulation included fringing fields and other spurious fields and losses that are not inherently important to this work. However, it is important to note that the full-wave simulation sill exhibited the same behavior - a constant, positive slope.

3.3.2 Transmission Line and Capacitor

For the next step in my analysis I added a capacitor in series with the line inductance of the transmission line. The dimensions of the capacitor are the same as those of the piezoelectric resonator, so we can explicitly observe the change in behavior when the resonant behavior is added later.

With the capacitor, C_1 in series with the line inductance, the impedance and admittance become:

$$\begin{aligned} Z_0 &= \omega L_0 - \frac{1}{\omega C_1} \\ Y_0 &= \omega C_0 \end{aligned}$$

The ABCD matrix of cascaded networks is simply the product of the ABCD matrices of those networks. Therefore, we model the transmission line with the capacitor in series as a transmission line (of half the length of the previous transmission line), in series with the capacitor, in series with an identical transmission line. The resulting ABCD matrix is:

$$\begin{bmatrix} A & B \\ C & D \end{bmatrix} = \begin{bmatrix} \cos\frac{\theta}{2} & jZ_0 \sin\frac{\theta}{2} \\ jY_0 \sin\frac{\theta}{2} & \cos\frac{\theta}{2} \end{bmatrix} \begin{bmatrix} 1 & \frac{1}{j\omega C_1} \\ 0 & 1 \end{bmatrix} \begin{bmatrix} \cos\frac{\theta}{2} & jZ_0 \sin\frac{\theta}{2} \\ jY_0 \sin\frac{\theta}{2} & \cos\frac{\theta}{2} \end{bmatrix}$$

$$= \begin{bmatrix} \cos\theta + \frac{Y_0}{2\omega C_1}\sin\theta & jZ_0 \sin\theta + \frac{1}{j\omega C_1}\cos^2\frac{\theta}{2} \\ jY_0 \sin\theta + \frac{jY_0^2}{\omega C_1}\sin^2\frac{\theta}{2} & \cos\theta + \frac{Y_0}{2\omega C_1}\sin\theta \end{bmatrix} \tag{3.5}$$

In Equation 3.5, θ is the phase shift across one unit cell of the transmission line. Therefore, the phase shift across each half piece of transmission line is given by $\frac{\theta}{2}$. The dispersion across the composite unit cell, γ is determined via Equation 3.2. The simulation results are shown in Figure 3-3. Note that this plot is of the real component of γ; the imaginary part is zero. This indicates that there is no propagation through the system; the signal is evanescent. This behavior is to be expected because the frequency is low, and the signal is being passed through a capacitor. As we can see in Figure 3-3, the real part of γ decreases as frequency increases. This is consistent with

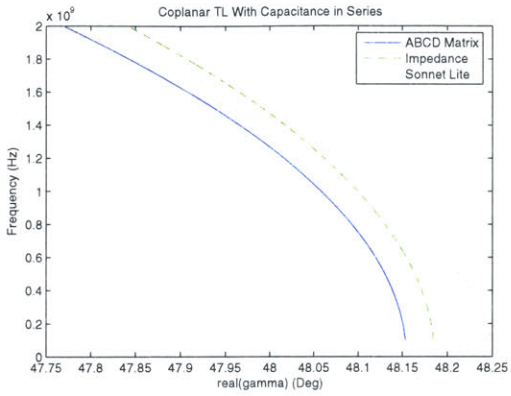

Figure 3-3: Loss through a transmission line with a capacitor in series.

the behavior of a capacitor, where the attenuation decreases as frequency increases, until a natural frequency, above which propagation will occur.

3.4 Proposed Metamaterial Structures

Now that we have methods for determining the dispersion through an arbitrary metamaterial circuit, we are able to analyze potential metamaterial architectures. First, we will place the resonator either in series with or across (shunting) a transmission line. We will observe the dispersion relations for these two structures to look for left-handed behavior. If one of these designs exhibits left-handded behavior, we will then be able to improve upon it to further analyze its potential.

3.4.1 Parallel

The Draper resonator is modeled as a Butterworth-VanDyke resonant circuit. Figure 3-4 shows the resulting circuit model when the resonator is placed across a transmission line of characteristic values C_0 and L_0. The resulting values of Z_0 and Y_0 are:

$$Z_0 = j\omega L_0 \tag{3.6}$$

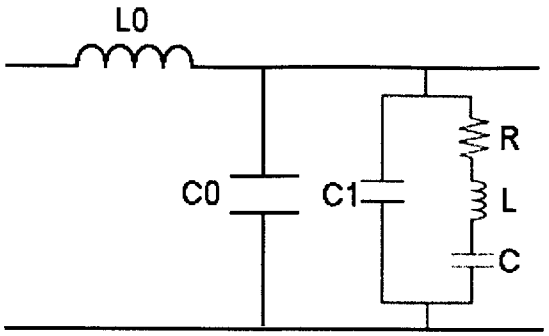

Figure 3-4: Equivalent circuit of a Draper resonator placed across a transmission line.

$$\begin{aligned} Y_0 &= \jmath\omega C_0 + \jmath\omega C_1 + \frac{1}{R + \jmath\omega L + \frac{1}{\jmath\omega C}} \\ &= \jmath\omega C_0 + \jmath\omega C_1 + \frac{\jmath\omega C}{1 + \jmath\omega RC - \omega^2 LC} \end{aligned} \tag{3.7}$$

If this structure is repeated periodically the dispersion relation will be described by Equation 3.3. Substituting the values of Z_0 and Y_0 produces:

$$\begin{aligned} \sin^2\frac{\theta}{2} &= -\frac{1}{4}\jmath\omega L_0 \times \jmath\omega\left(C_0 + C_1 + \frac{C}{1 + \jmath\omega RC - \omega^2 LC}\right) \\ &= \frac{\omega^2 L_0}{4}\left(C_0 + C_1 + \frac{C}{1 + \jmath\omega RC - \omega^2 LC}\right) \end{aligned} \tag{3.8}$$

Therefore, if many of the Draper resonators were to be periodically placed along a transmission line, the dispersion relation of the material described would follow the relation described by Equation 3.8.

To determine if the material produced by this method exhibits left-handed or otherwise interesting behavior, a graph of the dispersion relation (Equation 3.8) is created and analyzed. The graph of the dispersion relation was created using values gathered from analysis of the Draper resonators for C, L, R, and C_1. The values of C_0 and L_0 were then chosen to optimize the behavior of the material.

The dispersion relation of a left-handed material is characterized by phase and group velocities of different sign. Specifically:

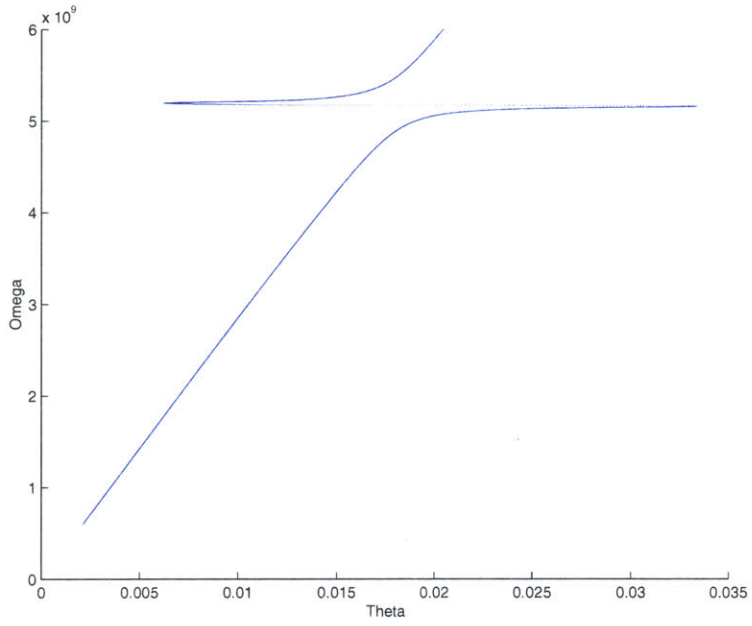

Figure 3-5: Dispersion relation of parallel architecture material.

$$\begin{aligned} v_{phase} &= \frac{\omega}{k} \\ v_{group} &= \left(\frac{\partial k}{\partial \omega}\right)^{-1} \\ v_{phase} v_{group} &< 0 \end{aligned} \tag{3.9}$$

On the graph of a dispersion relation, this requirement can be easily spotted when the slope of the plotted line at a point is of opposite sign than a line from the origin to that point. Looking at Figure 3-5, this happens near $\omega = 5 \cdot 10^9$. However, this is over a very small frequency range and a small change in frequency will result in a large change in phase shift. This behavior may not be ideal, so next we will explore a series architecture.

3.4.2 Series

To possibly achieve improved left-handed behavior, a series architecture was also modeled. An architecture of this type is realized by placing the Draper resonator in

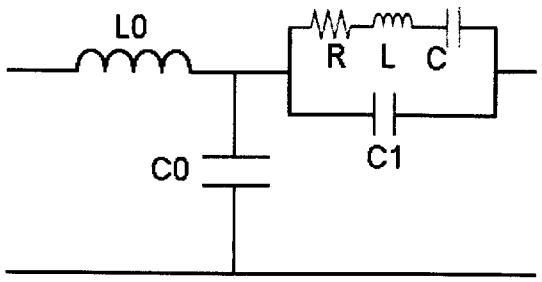

Figure 3-6: Equivalent circuit of a Draper resonator placed in series with a transmission line.

series with a transmission line of characteristic values C_0 and L_0. A circuit diagram of the resulting unit cell is shown in Figure 3-6.

Placing this unit cell in the lumped element model of a general line, we calculate the associated impedance, Z_0, and shunt admittance, Y_0.

$$Z_0 = \jmath\omega L_0 + \frac{1}{\jmath\omega C_1 + \frac{1}{R+\jmath\omega L+\frac{1}{\jmath\omega C}}} \tag{3.10}$$

$$Y_0 = \jmath\omega C_0 \tag{3.11}$$

These values are used in Equation 3.3 to produce the dispersion relation for a material produced with the series architecture.

$$\begin{aligned}\sin^2\frac{\theta}{2} &= -\frac{1}{4}\jmath\omega C_0 \times \left(\jmath\omega L_0 + \frac{1}{\jmath\omega C_1 + \frac{1}{R+\jmath\omega L+\frac{1}{\jmath\omega C}}}\right) \\ &= \frac{\omega^2 C_0}{4} \times \left(L_0 - \frac{R\omega C + \jmath\omega^2 LC - \jmath}{\omega^2\left(C_1 R\omega C + \jmath(C_1\omega^2 LC - C_1 + C)\right)}\right)\end{aligned} \tag{3.12}$$

Using the same values of C, L, R, and C_1 gathered from analysis of the Draper resonators, and adjusting L_0 and C_0 to achieve preferred behavior the dispersion relation of this material is analyzed.

Figure 3-7 represents the dispersion relation of a material constructed by period-

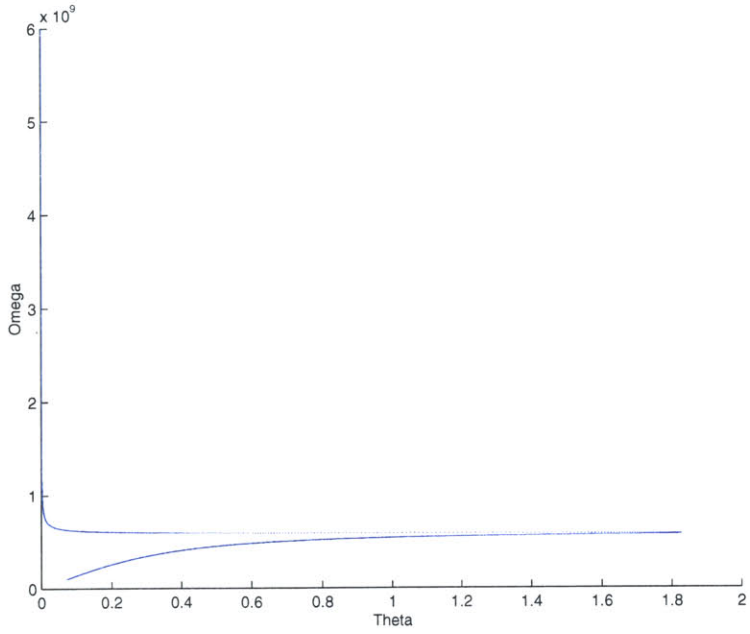

Figure 3-7: Dispersion relation of series architecture material.

ically placing the Draper resonator in series with a transmission line. In this graph, a left-handed behavior is evident above $\omega = 0.75 \cdot 10^9$.

Also, in Figure 3-7 there is another interesting behavior. As the frequency increases above $\omega = 1 \cdot 10^9$, theta approaches zero. As a result, the phase velocity approaches infinity. This shows that the phase shift across a unit cell approaches zero at high frequencies. Additionally, this behavior is present over a large range of frequencies. This behavior is beneficial because a wave consisting of many different frequencies will be able to propagate through the material without the different frequencies experiencing different delays. This effect, however, is due to the small size of the unit cell. If the phase shift per meter were plotted, (and scaled to ignore the huge phase shift at resonance), the material would most likely be dispersive. This effect is investigated in further detail in Section 3.8.

3.5 Boundary Condition Considerations

Due to the behavior of the resonators, the impedance presented at the end of the transmission line will also exhibit complex behavior that changes with frequency. It is important to note that all of these simulations assume an infinite array and therefore ignore boundary conditions. This is possible because we are merely assessing the ability to create the material, while the boundary condition considerations will become important when engineering a material for a specific application.

3.6 Microstrip Simulations

The initial designs that were considered placed the resonator in microstrip transmission line. This line is simply two parallel plates with a dielectric between them. This structure was used because it is the standard transmission line model, and was thought to be easy to fabricate. Figures 3-5 and 3-7 are from simulations of a microstrip architecture. However, in this design, it would have been difficult to access the ground plane with the network analyzer probes that I had access to, so a coplanar waveguide was used instead.

3.7 Coplanar Simulations

A coplanar waveguide (CPW) consists of three flat, coplanar, conducting lines. The inner line is the signal line, while the outer two are ground. The CPW is very popular due to the ease of access to the ground line and the ease of integration with surface-mount devices. Although it is not the standard line used in most equations that are used for modeling, it can be converted to the standard values via a conformal mapping, which is shown in Appendix A.1.

With the values for the transmission line parameters from Appendix A.1 and the equivalent circuit parameters for the resonator extracted in Chapter 2, we are able to produce a model of the resonator in series with a CPW. Therefore, we used the

values from the equations in Appendix A.1 in Equations 3.10 and 3.11 to determine the dispersion relation of the resonator in a CPW architecture.

After creating the model, we noticed that the resonator that was measured was actually fabricated in a CPW structure similar to the one that was modeled. So, while the dimensions of the fabricated CPW were not ideal for our model, it provided a great way to further ensure that our model was accurate.

First, I compared the measured S-parameters (which were directly output from the network analyzer used to test the resonators) to those from our model. The S-parameters for our model were obtained from the ABCD parameters through standard conversion equations from [33]. The ABCD matrix was obtained via a process similar to the one used for the transmission line and capacitor combination in Equation 3.5, but with the impedance of the resonator in place of the capacitor. The resulting S-parameters are shown in Figure 3-8. The model matches quite well with the measured values. The only disparity is that the measured values of S11 and S22 are less than the simulated ones. This could be due to some loss from impedance mismatch of the transmission line to the network analyzer that is not included in the BVD model.

With the model well-formed and its inaccuracies understood, we are finally able to plot the dispersion of the resonator and compare it to that of the measured values. Figure 3-9 shows the resulting plot, including results from the full-wave simulator, HFSS. Remember that gamma is the complex propagation constant, such that:

$$V(z) = V(0)e^{-\gamma z}$$

Therefore, the real part of gamma is the attenuation, and the imaginary part of gamma indicates the phase shift. So, when looking at Figure 3-9, the top plot is the percent of the signal transmitted, and the bottom is the phase shift. Note that less signal is transmitted through the measured devices than through the simulated ones. This is due to the loss that was seen in Figure 3-8. The large negative phase shift shown to be measured in the bottom of Figure 3-9 may be due to reflections from boundary conditions that are also not included in our models. While our model does

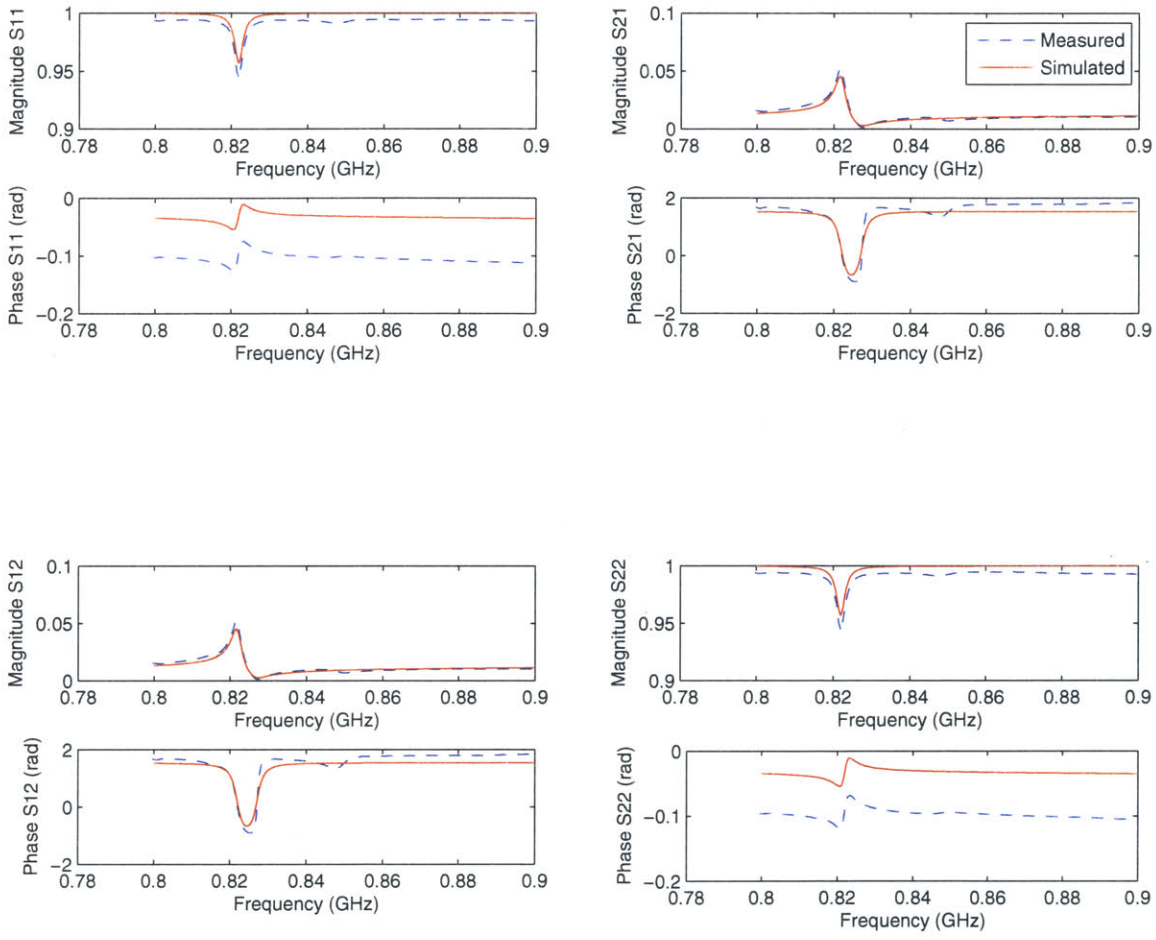

Figure 3-8: Measured and Simulated S-parameters.

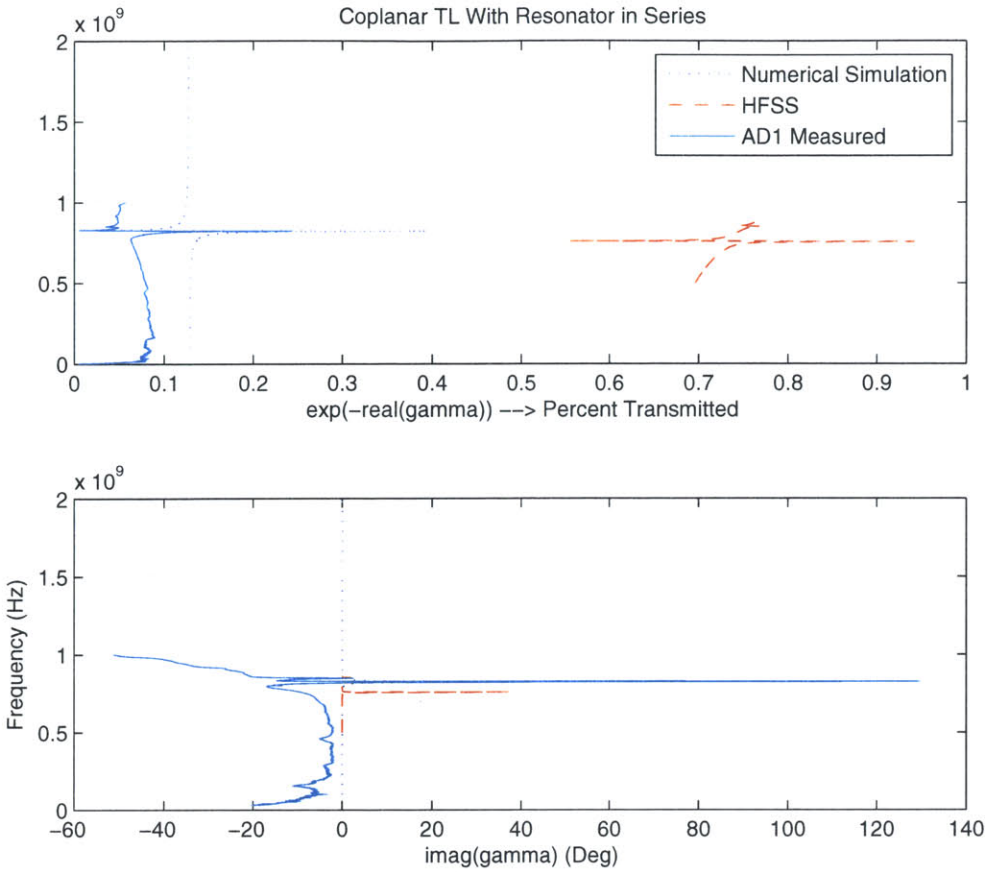

Figure 3-9: Percent transmitted and phase shift per meter of the designed metamaterial.

report a negative phase shift, it is of a much smaller magnitude.

3.8 Metamaterial Phase Shifter Simulation

With the results from our simulation, indicating that the designed metamaterial, a piezoelectric resonator in series with a coplanar waveguide, produces interesting phase shifting behavior, we can now design useful applications for this material. The first application considered is that of a phase shifter. Because our resonator can produce a phase shift much greater than its physical length, it may be a valuable system element.

3.8.1 Length

The first simulation for this application is to find the length that would be required to effect a 90-degree phase shift. It is quite simple to determine this length. We already solved for gamma, which is the phase shift per meter of the metamaterial. We simply divide 90 degrees by this value to obtain the length for a 90 degree phase shift. Note that to obtain an exact 90 degrees of phase shift may not be this easy. Because the unit cells each contribute a discrete amount of phase shift at a certain frequency, it is not possible to get fractional values of this discrete amount. However, it would be possible to get the phase shift as close to 90 degrees as possible and then add a length of transmission line to tune the phase shift to exactly the desired amount. In Figure 3-10, the length required for a 90 degree phase shift through a transmission line is plotted, as well.

3.8.2 Efficiency

While the metamaterial may be able to produce a phase shift in a small physical length, it is important to consider the efficiency of this device, as well. The percent of the signal that is transmitted is obtained from the real part of the propagation parameter, gamma, and the minimum length that was found from the top part of Figure 3-10. We used the minimum length to simulate the operation of an actual device.

The percent of a signal that is transmitted through the designed 90 degree phase shifter to a 50 Ohm load is plotted in the bottom part of Figure 3-10. The metamaterials (measured and simulated) both pass more than $1/10^{th}$ of the input signal. Also, note that the largest percent transmitted occurs at the frequency where the smallest physical length is required, making this operation point very beneficial. However, at slightly higher frequencies, the amount of signal that is passes reaches a minimum. However, this minimum is only approximately one order of magnitude less than the base value, and the signal is therefore still quite useful.

Because we are modeling a lossless transmission line, the percent transmitted

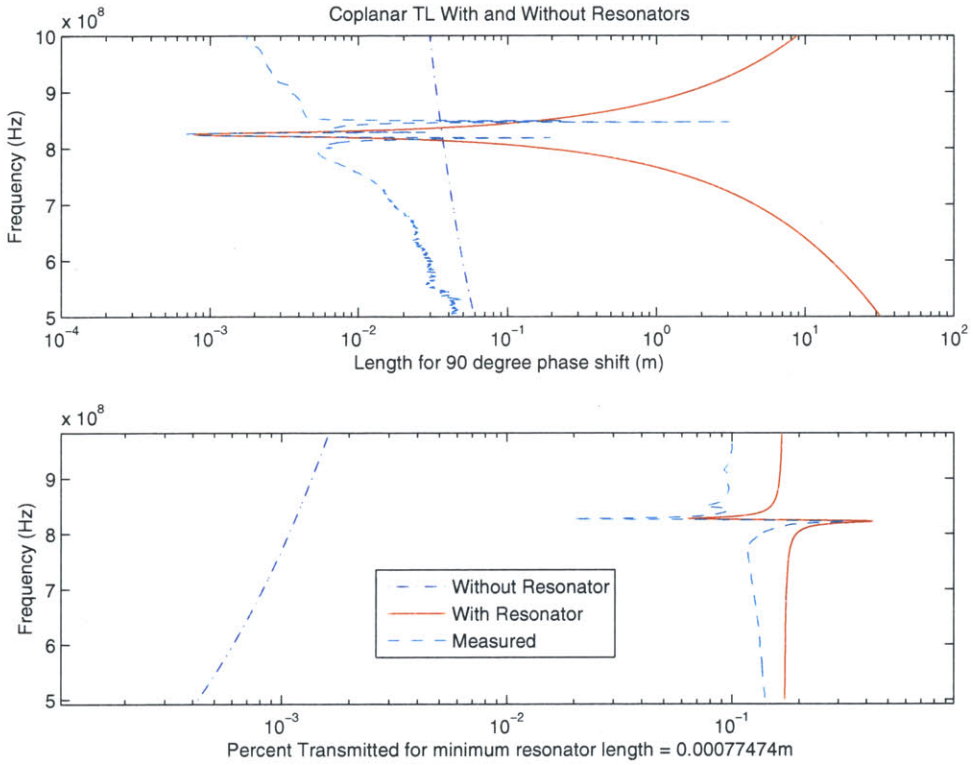

Figure 3-10: (a)Length required for 90 degree phase shift from a standard transmission line, a metamaterial transmission line, and the measured transmission line. (b) Efficiency of the three structures when all are the same length and driving a 50 Ohm load.

should theoretically be 100 percent for all frequencies (the 50 Ohm load is matched to the impedance of the transmission line). However, in Figure 3-10, when transmission lines become small with respect to a wavelength their complex impedance is dependant on their length and the frequency at which they operate. So, to evaluate the loss that would occur in a transmission line, I considered the complex impedance that would be created by a transmission line that was the same length as the phase shifting structure. The resulting impedance mismatch created by the transmission line creates the loss that is shown by the blue line in Figure 3-10.

3.9 Conclusion

In this chapter, we built a model of the piezoelectric resonator that can be used in larger systems. We tested this model on known systems to ensure its accuracy. Then, we designed several structures and utilized our model to simulate their behavior. This behavior was analyzed to determine if it would create the effects that we were looking for. The design consisting of a transmission line broken by the resonator in series showed a promising dispersion behavior.

Next we used this knowledge to analyze the dispersion characteristics of a metamaterial designed around the idea of the resonator in series with the transmission line. While most equations are based on the assumption of using microstrip transmission lines, a conformal mapping technique was used to be able to utilize a coplanar waveguide structure. Because the resonators that were fabricated and measured were in a coplanar architecture, we could then compare our modeled data to actual measured results.

After obtaining the dispersion relation for the designed metamaterial, we evaluated its effectivness as a phase shifting circuit element. The material seems to be very beneficial, producing a 90 degree phase shift in a size much smaller than would be required for a standard transmission line, while maintaining a useful efficiency.

THIS PAGE INTENTIONALLY LEFT BLANK

Chapter 4

Characteristic Parameter Analysis

Another important method of evaluating metamaterials is to consider the effective material parameters. As opposed to the dispersion analysis in Chapter 3, which modeled the periodic array of resonators and transmission lines as a periodic array of circuit units, the material analysis considers the material as a whole and determines the bulk material properties that it will produce. The material properties can then be used to determine many important things, including the impedance of the material, the velocity of wave propagation, and the resulting size of a quarter-wave patch antenna.

In this chapter we will extract the values for permeability and permittivity that will result from the structure that was designed in Chapter 3. Then we will examine how we can tune these values by changing the dimensions of the resonators used to construct the material. Finally, we will examine the usefulness of the metamaterial when considering its material properties and the resulting possible applications. [1]

[1]While reading this chapter, it is important to understand that MEMS devices may not exactly follow the rigid formulae that are generated. Changes due to altered anchor points, electrodes, fabrication tolerances, and numerous other minutiae are not included in this analysis and would require much work to fully characterize. This chapter does, however, provide a useful overview of the potential behavior of a MEMS metamaterial as well as a general design process that will produce metamaterial structures that can approach desired effective values.

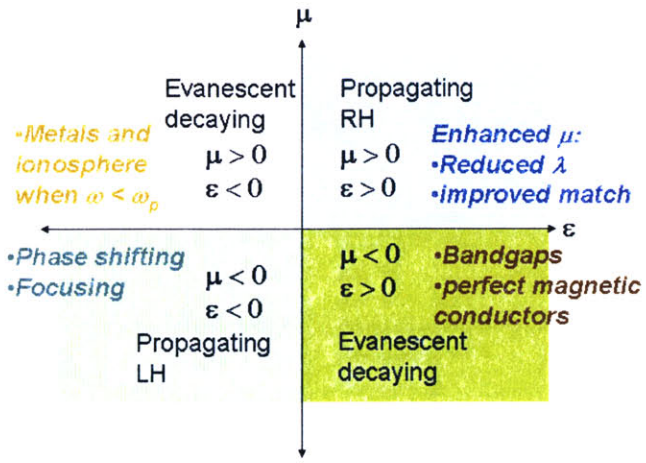

Figure 4-1: Example of ϵ versus μ space, with behavior and uses labeled for each quadrant.

4.1 Thinking About Material Properties

As described earlier, the parameters μ and ϵ determine much about the behavior of a wave in a material. Besides the impedance and wave velocity, which depend on the relations between μ and ϵ, the relative signs of these values specify what type of wave will exist in the material. Figure 4-1 displays the four possibilities of the sign combinations for μ and ϵ, encapsulated in the four quadrants of a plot with ϵ on the x-axis and μ on the y-axis. When μ and ϵ are of the same sign, the wave propagates (because the wavevector, which is $k = \omega\sqrt{\epsilon\mu}$, will therefore be real. When both μ and ϵ are positive, this is the standard, right-handed, propagation method that exists in most materials. When μ and ϵ are negative, as mentioned before, this is the left-handed propagation region. When μ and ϵ have opposite signs, the wavevector is imaginary, and the fields in that material decay very rapidly and are called "evanescent". This behavior is found in metals and plasmas when the frequency of the wave is less than the plasma frequency. Also, this behavior occurs for some frequencies in photonic bandgap materials.

Figure 4-1 also enumerates some applications where the material values in each quadrant can be useful. In the first quadrant, work is being done to adjust the values of μ and ϵ to improve impedance matching as well as reducing the wavelength (by

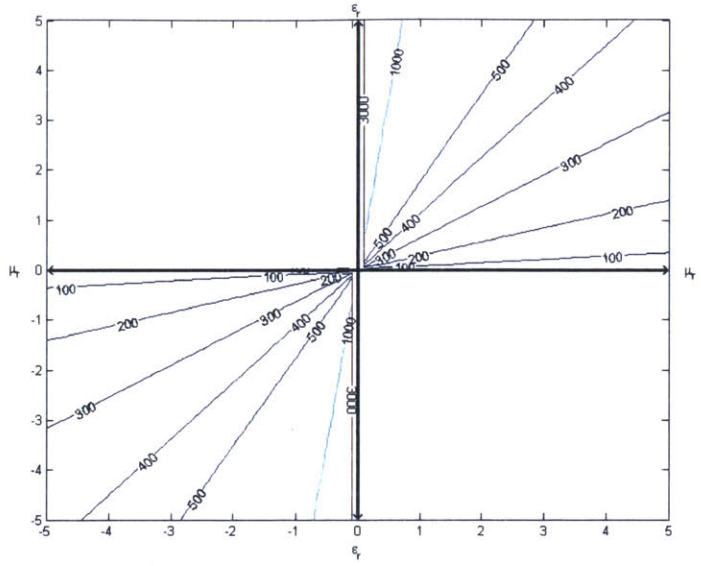

Figure 4-2: Real part of impedance in ϵ versus μ space.

increasing the wave velocity). The second and fourth quadrant create evanescent waves. This behavior can be used in antennas to suppress surface waves, which are a large source of loss in patch antennas. The third quadrant is the area that I am researching, whereby we can have backwards-traveling waves. This area can have useful applications in phase shifting and focusing of radiation.

Another material factor to consider is the impedance. Our materials can achieve a real as well as an imaginary impedance. The real impedance indicates how the magnitude of the current through a device is related to the voltage across it. The imaginary part of the impedance indicates the phase shift that is involved. When matching to a complex load, it is ideal for the impedance of the material to be the complex conjugate of the load. Since free space has a purely real impedance, however, we would ideally have a purely real impedance. Figure 4-2 shows the real part of the impedance, $Z = \sqrt{\frac{\mu}{\epsilon}}$, plotted for the relative values of permittivity and permeability. Note that in quadrants two and four, the impedance is purely imaginary.

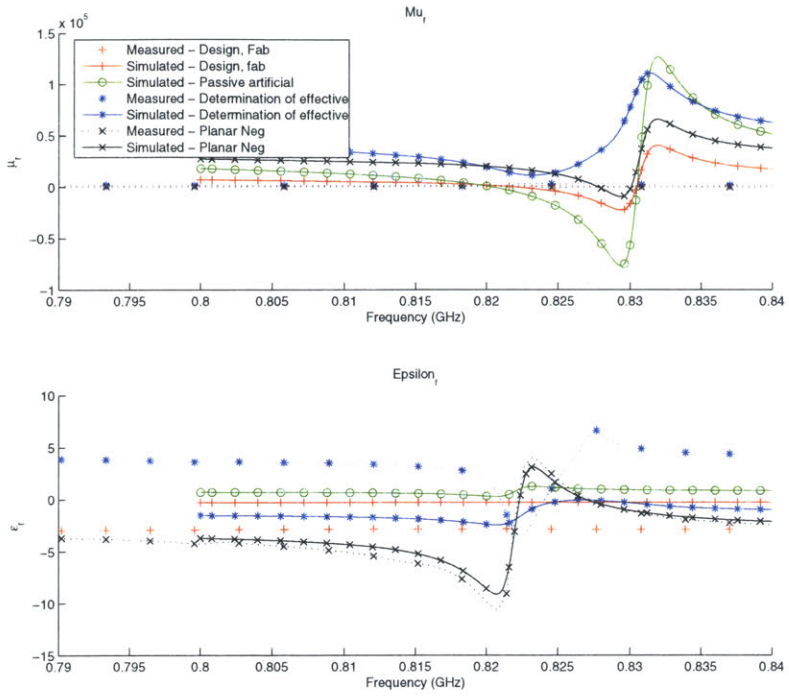

Figure 4-3: Extracted measured and simulated material parameters via several different methods.

4.2 Extraction of Characteristic Parameters

The extraction of the permittivity and permeability of a metamaterial is an important process, as these values can embody much of the behavior of the material. It is important to verify that the extraction is done correctly. Therefore, I performed the extraction via four different methods and used each of their behaviors to verify the accuracy of the others. Then I choose the most robust method with which I can perform further analysis of the metamaterial.

4.2.1 Methods of Extraction

There are several methods that have been used to extract the effective material parameters from scattering matrix (S-parameter) data. Because the extraction process requires taking roots and inverse trigonometric functions, the person performing the extraction must choose the proper roots for each method. Because in the analysis

of left-handed materials, the accuracy of the signs is very important, I analyzed four methods and used the similarities among their behaviors to verify their accuracy.

NRW Method

The lines in Figure 4-3 labeled "Design, Fab" indicate that they were obtained using the Nicolson-Ross-Weir (NRW) approach, similar to that used in [40], and laid out in [11] and [2].

In this method, we define the composite terms:

$$\begin{aligned} V_1 &= S_{21} + S_{11} \\ V_2 &= S_{21} - S_{11} \end{aligned} \tag{4.1}$$

From which we derive expressions for the impedance and admittance of the structure. The values of impedance and admittance can then be used to determine the transmission and reflection coefficients, which can, in turn be used to determine the index of refraction and the wavevector, which are used to produce expressions for the permeability and permittivity. The resulting equations that I used were:

$$\begin{aligned} \mu_r &\approx \frac{2}{jk_0d}\frac{1-V_2}{1+V_2} \\ \epsilon_r &\approx \frac{2}{jk_0d}\frac{1-V_1}{1+V_1} \end{aligned} \tag{4.2}$$

NRW Variant

A variant of the NRW approach, used in [36], is indicated by the light blue and black lines in Figure 4-3 and the label "Determination of Effective." In this method, as in the previous one, the transmission and reflection coefficients are used, but the equations to extract the impedance and the index of refraction are different. The values are obtained as follows:

First we calculate T and Γ, the transmission and reflection coefficients, the wavevector of the incident wave, $k = \omega/c$, and the normalized transmission coefficient,

$T' = Te^{-jkd}$. Then, we use Equation 4.3 to find the imaginary part of the index of refraction. In these equations, d is the length of the material.

$$Im(n) = \pm Im\left(\frac{\cos^{-}1\left(\frac{1}{2T'}[1-(\Gamma^2-T'^2)]\right)}{kd}\right) \tag{4.3}$$

We solve the right-hand-side and take whatever root yields a positive solution for $Im(n)$. The requirements that $Re(z)$ and $Im(n) > 0$ are for all passive materials. The real part of n is determined from:

$$Re(n) = \pm Re\left(\frac{\cos^{-}1\left(\frac{1}{2T'}[1-(\Gamma^2-T'^2)]\right)}{kd}\right) + \frac{2\pi m}{kd} \tag{4.4}$$

The equation for the real part of n is complicated by branches of the arccosine function. In Equation 4.4, m is an integer. The values for ϵ and μ are then determined using the identities:

$$\epsilon = \frac{n}{z}, \qquad \text{and} \qquad \mu = nz$$

Note that in this method of parameter extraction, the requirement that $Im(n) > 0$ uniquely identifies the sign of $Re(n)$ [36]. This characteristic is very valuable in our analysis, as it disambiguates the left-handed areas by specifying the sign of the index of refraction. Because the index of refraction is negative in left-handed materials, this explicit specification ensures that we are observing left-handed behavior, and not just taking the desired root of the characteristic equations.

Because of this explicit stipulation that results in unambiguous handedness of the resulting material (and signs of the permittivity and permeability) this method (the adjusted NRW method used in [36] will be the primary method of analysis used in the later portions of this chapter.

Polarization and Susceptibility

Permittivity and permeability describe the interaction of a material with electric and magnetic fields. This behavior is dependent on the ability of the fields to polarize

particles in that material. Therefore, another method to extract the effective material parameters is to analyze the susceptibility of the material. This method is used in [37].

The permeability of a material is $\mu = 1 + \chi$, where the magnetic susceptibility, χ, can be obtained by modeling each unit cell of our material as an electrically small, loaded dipole antenna [41]. Using the Thevenin equivalent circuit of this antenna, we know that the current across the terminals of this component due to a V_{OC} induced by an incoming electric field is:

$$I_{\mathrm{in}}(\omega) = I(z = 0) = \frac{V_{\mathrm{OC}}}{Z_{\mathrm{in}}(\omega) + Z_{\mathrm{L}}(\omega)} \tag{4.5}$$

The susceptibility is then described by:

$$\chi_e(\omega) = \frac{K_e}{-j\omega[Z_{\mathrm{in}}(\omega) + Z_{\mathrm{L}}(\omega)]} \tag{4.6}$$

Where the positive constant factor K_e is defined as:

$$K_e = \frac{l_0^2}{\epsilon_0 V} \cos\psi_e \sin\theta \tag{4.7}$$

In these equations, l_0 is half of the physical length of the antenna (in our case the unit cell), ψ_e is the polarization angle between the dipole and the electric field, which we assumed to be 0, as we are only considering a linear system, and V is the effective volume in which the calculated composite permittivity is constant. After substituting the load and input impedances of our device (the large expression for Z used earlier and 25 Ohms, respectively) into the above equations, we can calculate the permeability, μ. With the permeability, we can use the index of refraction or the impedance calculated via another method to determine the permittivity, ϵ.

Circuit Analysis

The lines labeled as "Planar Neg" in Figure 4-3 refer to the method used in [8]. This method utilizes the circuit model of the material and uses those values to extract the

material parameters from electromagnetic field equations. These field equations are mapped from the circuit telegrapher's equations via Ampere's law and the definition of potential. The permittivity and permeability are therefore related directly to the per-unit-length capacitance and inductance of a line.

The telegrapher's equations are the standard equations relating current and voltage in a transmission line with impedance and admittance, Z and Y, respectively.

$$\frac{dv}{dx} = -iZ, \qquad \frac{di}{dx} = -vY$$

The field equations are therefore:

$$\frac{dE}{dx} = -j\omega\mu_S H, \qquad \frac{dH}{dx} = j\omega\epsilon_S E$$

Which yield expressions for the effective material parameters:

$$\mu_S = \frac{Z}{j\omega}, \qquad \epsilon_S = \frac{Y}{j\omega}$$

4.2.2 Method Comparison

When plotting the values of μ and ϵ obtained via each different method, I chose the roots of the equations that I used so they all would agree. The method that I trusted the most to have accurate signs was the adjusted NRW approach, as it had explicit stipulations for the choice of the proper sign. Therefore, in most cases, I chose signs in the other methods to match that of the NRW variant.

Therefore, the NRW Variant from [36] was the parameter extraction method that I used primarily for the further analysis that follows.

4.3 Values Accessible through MEMS Metamaterial

Given a robust method for extracting the permeability and permittivity of the designed metamaterial, we can analyze what values are achieved via the proposed material. Then, we can vary design parameters in our model to determine the ability of a MEMS metamaterial achieve different ranges of μ and ϵ.

4.3.1 Material Parameter Extraction

The process for the extraction of the permittivity and permeability was described earlier in this chapter. The real part of the extracted values for the material using the measured resonators is shown in Figure 4-4. The top two pieces of this figure are the relative permeability and permittivity, while the bottom graph shows these two parameters plotted together. Note that while the scale is different for the two plots in the bottom piece, their respective zero points are aligned. Figure 4-4 is similar to Figure 4-3, except it only uses one method (the NRW variant). Additionally, in Figure 4-4, the zero line is marked. When the value of permittivity drops below this line, both values are negative and the material will behave as a left-handed material.

Figure 4-5 shows the same data, but in a different manner. The top two plots of permittivity and permeability are the same as the previous figure, but the next two pieces are shown differently. The middle plot shows the values of permittivity versus permeability. The plot of μ versus ϵ is very valuable, as it captures the behavior of the material as shown in Figure 4-1. Specifically, this plot contains the second and third quadrants of Figure 4-1. Therefore, when looking at Figure 4-5, it is important to remember the behavior of materials that will result from different positions in this space. We will therefore be using this type of plot throughout the rest of this chapter.

An additional piece of data contained in Figure 4-5 is the frequency. It is important to note that the values of μ and ϵ achieved by the material are valid for only a specific frequency. The bottom piece of Figure 4-5 captures this behavior. We can see that

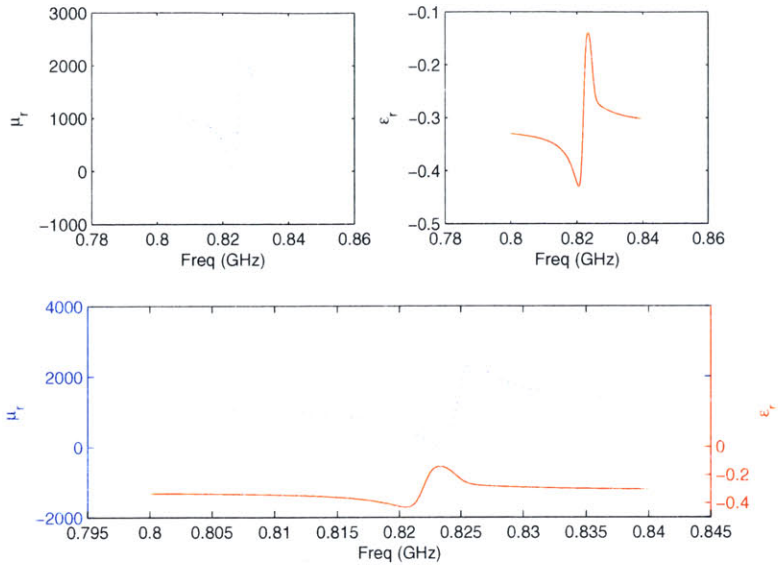

Figure 4-4: The extracted permittivity and permeability of the resonator.

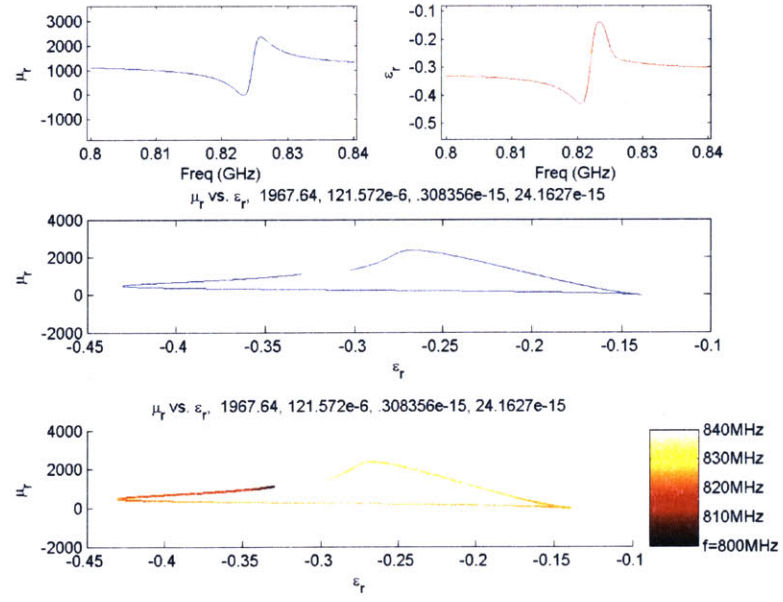

Figure 4-5: Permittivity and Permeability of a resonator metamaterial with the frequency of operation indicated.

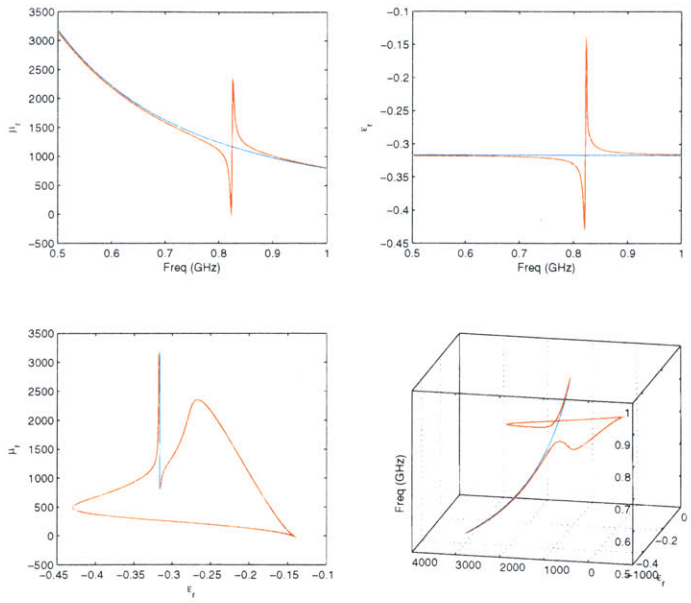

Figure 4-6: Permittivity and Permeability of a resonator metamaterial and a capacitor plotted against frequency.

there are values of μ and ϵ that we converge to at high and low frequencies, but when we are near the resonant frequency of our resonators, we can achieve many different material properties. However, this also shows that there is a very narow bandwidth for these properties. A small change in frequency can result in a large change in μ and ϵ.

Figure 4-6 plots the same data once again, but with one further variation. The top two plots are once again the permittivity and permeability, but this time they are plotted over a much wider frequency range. Also, the light blue line is the values of μ and ϵ that would be produced by a material that was created using a capacitor in place of the MEMS resonators. Therefore, the blue lines show how the material would behave without the resonant behavior of the MEMS device. This line is a valuable piece of data so we can compare the two results and explicitly see what aspects the resonant behavior adds to the material.

The lower left plot is the same plot of permittivity versus permeability as in Figure 4-5, but again with the capacitor material data added. Finally, the lower right

portion of Figure 4-6 displays this data in three dimensions. This is equivalent to the coloring from Figure 4-5, but the third dimension representing the frequency is spatial, instead of color. This 3D representation also facilitates the comparison of the resonant material to that of the capacitor material. We can see how the resonant material follows the same path for most of the frequency range, but takes a range of different values around the resonant frequency before re-aligning with the capacitor at high frequencies.

4.3.2 Circuit Adjustment

Now that we can model, observe, and understand the material behaviors of a meta-material, we can see how changes in the resonant elements might effect the behavior of the bulk material. In this first section we will see how changes in the circuit elements of the resonator BVD model will effect the behavior of the material. It is important to remember that these changes are not physical, instead they are used to build an intuition to how the behavior can change. This intuition will then be utilized to understand the changes that will result from physical changes in the resonator.

The first circuit element that we chose to change is the parallel capacitor (C0). Figure 4-7 shows the resulting material values across a frequency sweep for five discrete capacitances. The top two pieces show the permeability and permittivity as usual. It is good to see that the change in parallel capacitance does not shift the resonant frequency much (as we would expect). It is interesting to see that increasing the parallel capacitance decreases the magnitude of the resonant behavior in the permeability, but increases the magnitude of the steady -state permittivity, with no change in resonance magnitude.

The bottom piece of Figure 4-7 shows the values plotted as permittivity versus permeability. While this plot may look confusing, recall that it is just the same as in all the previous figures, except that there are lines for several materials in the one plot.

The next circuit parameter that we swept was the series capacitance. The result is shown in Figure 4-8. This change basically only shifts the resonant frequency of

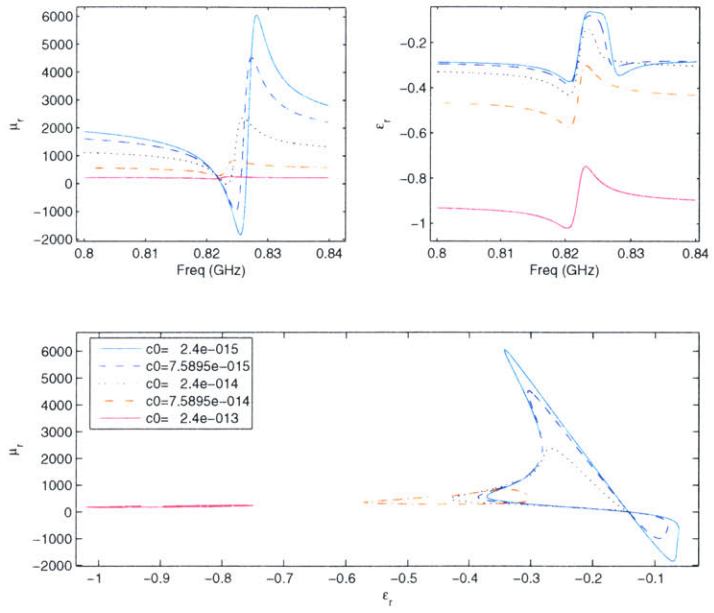

Figure 4-7: The extracted permittivity and permeability of several resonator metamaterials with different parallel capacitances.

the material, as can be seen in the top two plots. Also, the bottom plot demonstrates this behavior, as the lines for each different material are basically the same in two dimensions. Remember, however, that each line will achieve a given μ and ϵ at a different frequency. Also, because the inductor is in series with this capacitor, changing the value of the inductor will have a similar effect on the response of the material. The change, however, should be in a different direction due to the differences in the definition of impedance for the different circuit elements. When changing the value of the inductor, the resonant frequency should shift as with the capacitor, an increase in inductance should result in a lower resonant frequency.

4.3.3 Dimension Adjustment

The previous section was written to provide an intuition into how changes in the BVD circuit parameters can change the behavior of our metamaterial. However, as we mentioned in that section, these changes are not physically possible. What we

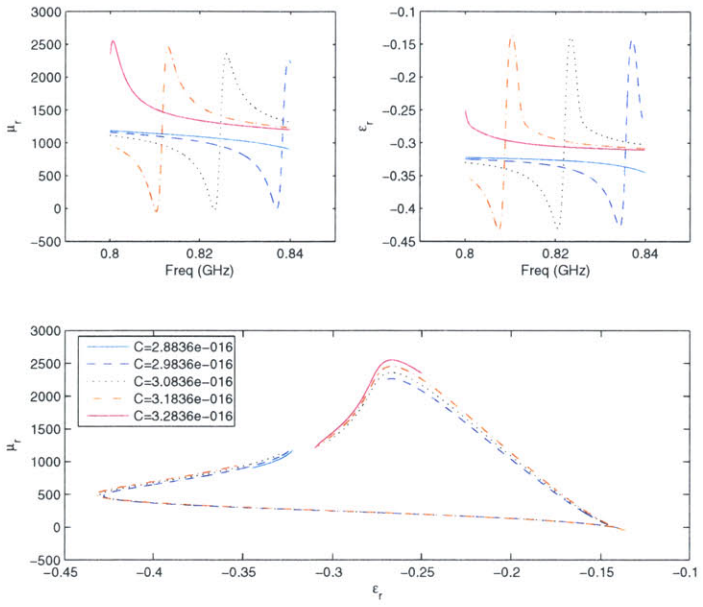

Figure 4-8: The extracted permittivity and permeability of several resonator metamaterials with different series capacitances.

can change is the dimensions of our resonator. Changes in these dimensions do not just effect one BVD circuit parameter, but several. So, in this section, we will show how the adjustment of dimensions of the resonator will change the values in the BVD model. Using this information along with the intuition that was built in the previous section, we will see how we can achieve different values of permittivity and permeability by changing the dimensions of our resonator.

We could first consider the resonator as two parallel conducting plates. From standard electrostatic equations, we know that capacitance is proportional to the width and length of the plates, and inversely proportional to the separation of the plates. The inductance is proportional to the plate length and separation, but inversely proportional to the width. From [15], we know that these relations hold with our resonator.

To find the BVD circuit parameters that would model a resonator built with specific dimensions, we adjusted the parameters extracted from the measured devices. Then we factored out the dimensions of the measured device and scaled by our new

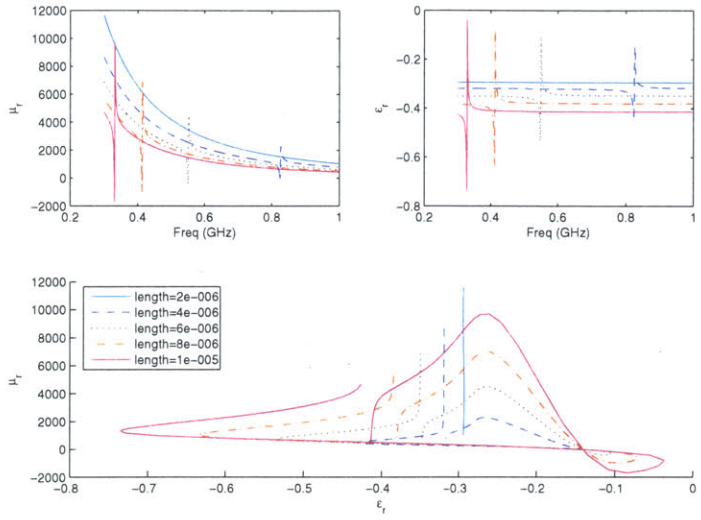

Figure 4-9: The extracted permittivity and permeability of several resonator metamaterials with different resonator bar lengths.

dimensions. We were then left with circuit parameters that should describe the new resonator. Placing these resonators in a periodic array creates a metamaterial that we can now analyze.

Now we can plot the values of permittivity and permeability for several choices of dimension, just as we did for the choices of circuit element value. The first dimension that we changed was the length of the resonator bar. From electrostatics, we would conjecture that an increase in the length of the resonator would result in both an increased capacitance and an increased inductance. Therefore, we would assume that the resulting permittivity and permeability would have shifted as well as scaled resonances. More specifically, an increase in length should decrease the resonant frequency and increase the magnitude of the resonance. Additionally, the permittivity should be shifted more negative for increasing values of length. Our intuition is correct, as this is the behavior that we see in Figure 4-9.

The bottom part of Figure 4-9 plots this data once again in the permittivity versus permeability space. Note how you need the proper parameters to actually achieve left-handed behavior. Figure 4-10 plots the same data as Figure 4-9, but in three dimensions. The third dimension is frequency. In this plot, you can see more

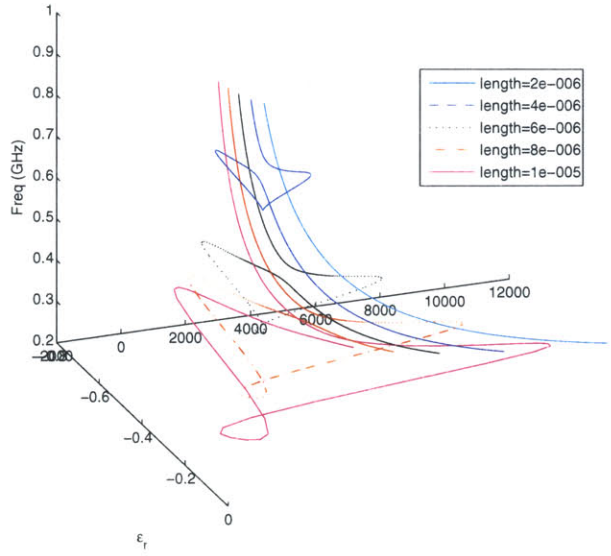

Figure 4-10: Three-dimensional view of the extracted permittivity and permeability versus frequency of several resonator metamaterials with different bar lengths.

accurately what material parameters are accessible at certain frequencies. The 3D representation also lets us see the bandwidth of the achieved material parameters. A line that is very flat in the plane of permittivity and permeability indicates that small changes in frequency will result in large changes in these values. The longer lengths or resonator seem to fit this description. The shorter widths, however, appear more stretched in the frequency dimension. This indicates that the change in permeability and permittivity due to a change in frequency is not as large for these materials. However, because we are working at a higher frequency, and the axis on Figure 4-10 is linear, the fractional bandwidth of the materials constructed with shorter resonators is approximately the same as one built using longer resonators.

Our next analysis will involve holding the length of the resonator bar constant and changing the values of the width. We would expect an increased width to increase the capacitance but decrease the inductance. Depending on the relationship between the changes of the series capacitor and inductor, it is unclear how this change will affect the resonant frequency, but we know from the change in parallel capacitance

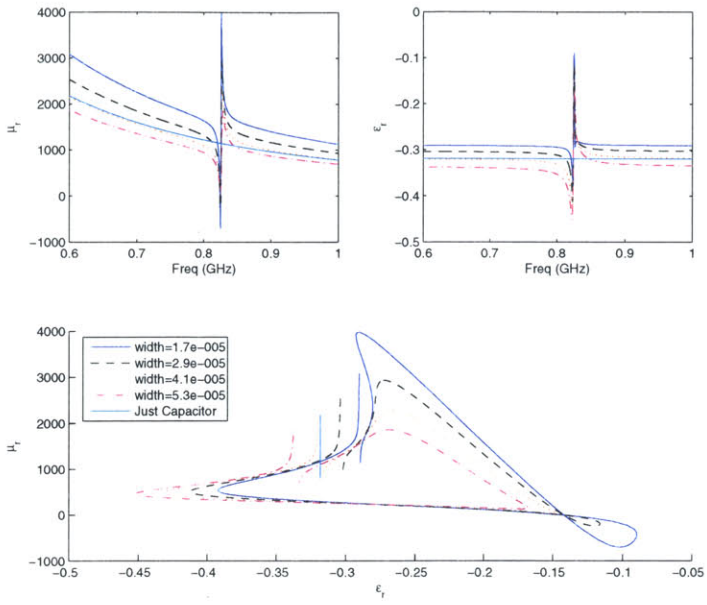

Figure 4-11: The extracted permittivity and permeability of several resonator metamaterials with different resonator bar widths.

that the magnitude of the resonance and the permittivity will decrease.

Figure 4-11 shows the values of μ and ϵ that are produced by a material constructed out of unit elements using MEMS resonators with the indicated widths. The first thing that we notice is that the resonant frequencies are all the same. This is very interesting; the frequency shifts that would result from the changes in series inductor and capacitor have canceled.

Figure 4-12 depicts the same data as Figure 4-11 , once again represented in three dimensions. It is interesting to see how all the materials follow the same frequency behavior, but the magnitude of their resonances and their starting positions are simply changed.

One addition to Figures 4-11 and 4-12 is that of the capacitor material, indicated once again by the light blue line. As in figures earlier in this chapter (like Figure 4-6) this line is the data that would be gathered from a material constructed from a periodic array of unit cells with a capacitor in place of the MEMS resonator. It follows the same path of our metamaterial, but with out the resonant behavior.

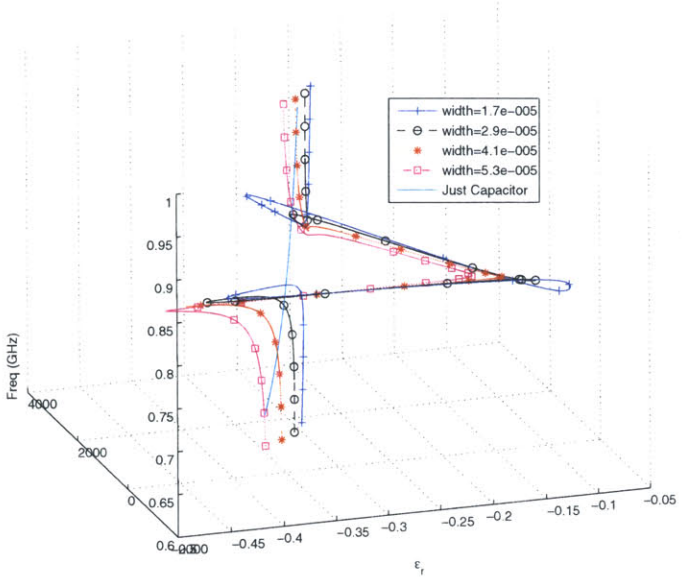

Figure 4-12: Three-dimensional view of the extracted permittivity and permeability versus frequency of several resonator metamaterials with different bar widths.

4.3.4 Accessible Values

Now, if we sweep both length and width, we can discover all the possible values of permittivity and permeability that can be produced by a metamaterial of our designed structure. We swept length and width exactly as before, but now plotted all possible combinations on one plot. Figure 4-13 is the result.

In Figure 4-13, note that the different widths are each denoted with a different color line. Therefore, the visible vertical groupings correspond to a single length, and the contracting paths within those groups correspond to different widths.

4.4 Applications

There are several practical uses for the versatile permittivity and permeability of this new MEMS metamaterial. In this section we will introduce a design process by which a desired value for μ and ϵ can be achieved at a specific frequency. Following the design process, applications where this ability could be useful are introduced.

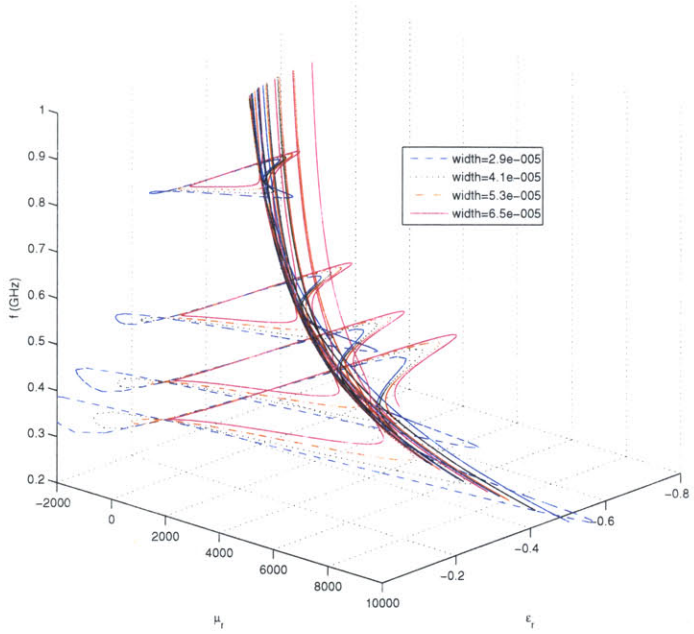

Figure 4-13: Three-dimensional view of the extracted permittivity and permeability versus frequency of several resonator metamaterials with varying bar widths and lengths.

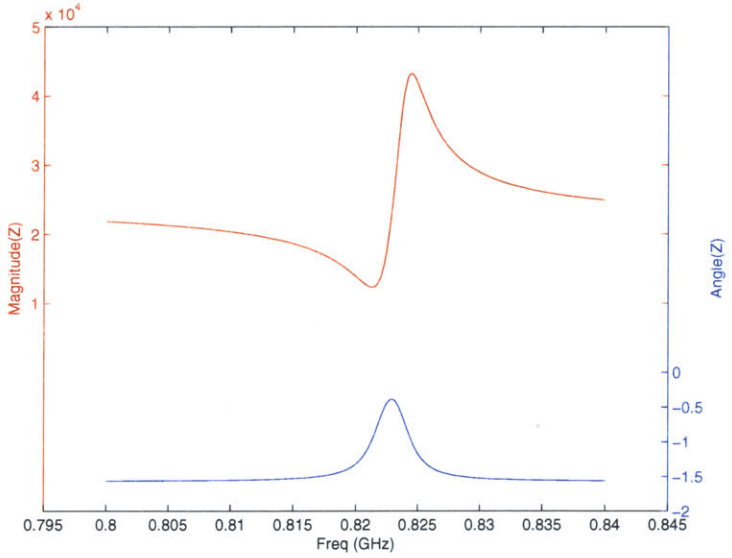

Figure 4-14: Impedance of MEMS metamaterial.

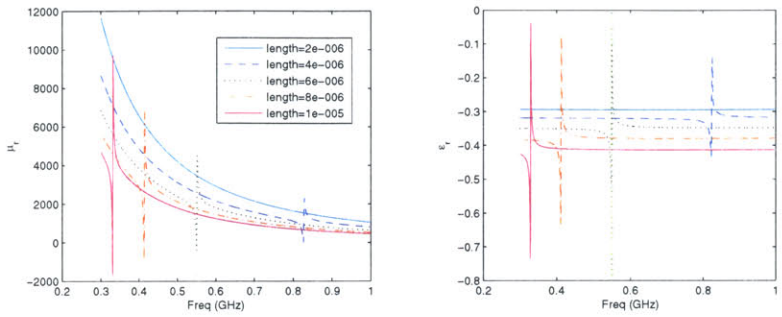

Figure 4-15: Selecting the length of the resonator by specifying the resonant frequency.

4.4.1 Design Process

We now have a method for determining the permittivity and permeability of a metamaterial constructed from a periodic array of piezoelectric MEMS resonators and coplanar waveguides. In this section we strive to make that ability useful by presenting a method, by which one can construct a material that will have chosen values of μ and ϵ at a specific frequency.

To design a metamaterial, you will first need to choose its frequency of operation. This will be the frequency where it will achieve the left-handed behavior, and is therefore the resonant frequency of the MEMS resonators that consist the material. We showed earlier in this chapter that the resonant frequency of the material is determined by the length of the resonator bars. Therefore, once you have chosen the desired frequency of operation, using the models created earlier in this chapter, you can determine the length of the resonator that should be used. This process is shown in Figure 4-15. We have chosen to operate around 550 MHz, and by looking for a plot that has a resonance there, we predict that the length of our resonators should be approximately 6 μm.

After a length is chosen, the width can be adjusted to achieved the desired material parameters. These parameters can be permittivity, permeability, or impedance. These three material values are plotted for different widths through a narrow frequency range around the operating frequency in Figure 4-16. The designer can then select a width of the resonator by choosing the desired impedance or μ and ϵ.

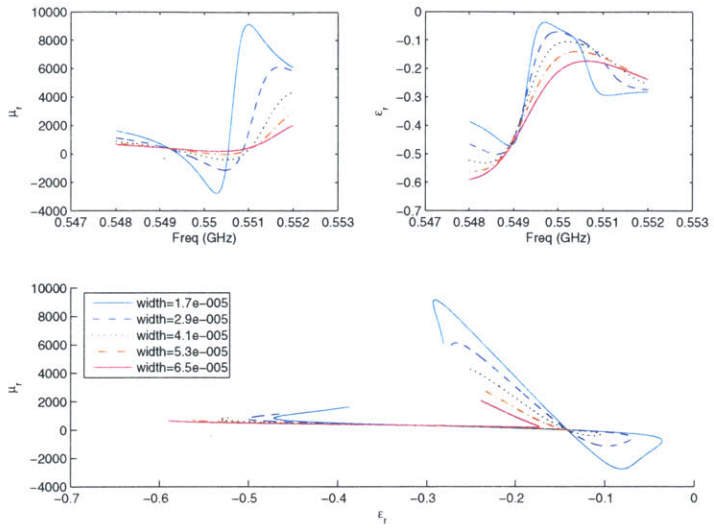

Figure 4-16: Selecting the width of the resonator by specifying the desired impedance and material parameters.

4.4.2 Improved Patch Antenna

There are several manners in which the MEMS metamaterial may contribute to the creation of an improved antenna. First, due to the increased phase shifting behavior mentioned before, it may be possible to decrease the size of a patch antenna. Because patch antennas should be resonant structures, their dimensions are dictated by the length needed to achieve a specific phase shift. Because we can achieve a phase shift through a smaller length, it may be possible to construct a smaller patch with similar resonant behavior.

A second manner of antenna application that was considered was the suppression of surface waves. Just as the size of a patch antenna is determined by the frequency, its depth follows the same dependency. As a result, the separation between a patch and its ground plane is increased to improve the efficiency of an antenna. However, there are currently several problems with this process. First, many patch antenna designers simply do not have the space to increase this dimension. Because the patch antenna is commonly integrated on a circuit board, it is not convenient to increase the thickness of this board. The improved phase shifting and the increased

impedance of our materials may constitute a material that will improve the efficiency of a patch antenna for a given thickness. However, the inherently planar structure of the resonator makes it difficult to apply in this manner. Other materials are most likely more cost-effective for this application.

The second problem faced when increasing the separation between a patch and its ground plane is the loss of power through surface waves along the substrate. Surface waves are actually the source of most of the loss associated with a patch antenna. If we could suppress these waves (while maintaining proper impedance matching between the feed, patch, and freespace), it would improve the efficiency of patch antennas. Our MEMS material has the properties that it will suppress waves at certain frequencies so it may be a good candidate for this application. However, there are many other materials that also accomplish this task. Photonic band gap materials can be constructed by having periodic metal inclusions or holes in a substrate in order to suppress waves at a certain frequency. These materials seem to be easier and less expensive to produce than the MEMS metamaterial, and may therefore be a better solution for surface wave suppression in patch antenna substrates.

A final potential improvement in antennas that can be accomplished through the utilization of a MEMS metamaterial would be at the ground plane. The separation of the antenna and its ground plane is necessitated by the use of a conducting ground plane. The reflections of the waves off of this plane are out of phase with the incoming waves, requiring a spacing of a quarter of a wavelength in order for the reflected wave to be in phase with the signal when it returns to the antenna. If a Perfect Magnetic Conductor (PMC) were used as the ground plane, the reflection would be in phase, and the separations between the antenna and the ground plane could be very small. A PMC is an artificial construct that would suppress electric field waves across its surface. Practical implementations nearing the behavior of a PMC have been called High Impedance Surfaces. It is possible that our MEMS structure would be very efficient at suppressing surface waves along a ground plane. The coplanar architecture that characterizes the resonators lends itself well to the construction of such a surface. It could therefore provide an effective manner of accomplishing a PMC, increasing

the efficiency of antennas while decreasing their size.

THIS PAGE INTENTIONALLY LEFT BLANK

Chapter 5

Conclusion

In this thesis I have analyzed the potential of a metamaterial constructed with MEMS resonators. My initial assumption was that the metamaterial would be constructed of a periodic array of MEMS resonators. Due to the resonant characteristics of the devices, many interesting behaviors can be produced. It was the goal of this thesis to further explore these potential behaviors by modeling potential metamaterial structures, determining their behaviors, and then analyze these behaviors. The metamaterial behaviors were analyzed by comparing their performance in chosen applications to that of existing technology.

To construct a metamaterial, I first had to choose the resonator to use. Through rigorous electrical and mechanical resonance analysis, I compared two types of resonator: the paddle resonator and the piezoelectric resonator. The piezoelecrtic resonator displayed a much lower impedance than the paddle throughout the entire frequency range. Also, the resonant peak of the piezoelectric resonator is much larger than that of the paddle. Therefore, it was concluded that the piezoelectric resonator would be the preferred MEMS resonator for the construction of a metamaterial.

After a resonator was chosen, various designs were considered. To model each potential design, I constructed a circuit abstraction that was equivalent to the MEMS resonator. This circuit was placed in various configurations within a transmission line. In this manner I simulated the behavior of an infinite array of these unit cells. By using many modeling techniques and refining the modeling process through several

structures, a robust model was created. The dispersion relations for each modeled structure were analyzed and compared with data collected from measured devices as well as the various modeling techniques. It was found that a resonator placed in series with a coplanar waveguide can produce left-handed behavior.

Using that structure, several applications were considered. Because the phase shift across the material can become very large at a resonant frequency, the first application that was considered was the use of the material in a phase shifting circuit element. This element was shown to potentially achieve a ninety degree phase shift at a size that is two orders of magnitude smaller than the required length of transmission line. Additionally, this phase shift occurs at a frequency where the impedance of the structure is at a minimum, making this result not purely academic, but viable for use in a circuit element.

The second application that was considered was the use of this material as a substrate for an antenna. The ability to choose the material parameters through the design of the material would be valuable for phase matching, size reduction, or efficiency improvement of small antennas. Analysis of this application required further model refinement to extract the values for the permittivity and permeability of the material. Several methods to achieve this were considered and refined to determine the material values for a given set of resonator dimensions. A method was presented by which an engineer can design a material for a given permittivity and permeability at a specific frequency.

5.1 Future Work

It is my conclusion that a MEMS metamaterial could produce vast improvement over existing technology in several areas. There are, however some problems that may need to be addressed or designed for before an application using a MEMS metamaterial is feasible.

5.1.1 Problems to Address

There are two problems with the current MEMS metamaterial structure that was considered; high impedance and narrow bandwidth. If this metamaterial is to be used as a medium for electromagnetic propagation, it will attenuate the signal by a large amount. This is an issue to consider when thinking about potential applications.

The second problem with the metamaterial is its narrow bandwidth. While many desirable behaviors are achievable through the use of the MEMS metamaterial, they usually only occur over a very narrow frequency range. This restricted region of operation can make it difficult to create a useful structure. There are two solutions to this problem that should be explored. First, by combining several of the resonators, we may be able to design our structure for improved bandwidth. This is a similar concept to combining multiple resonators to create a multi-pole wideband MEMS filter. The second solution to the bandwith problem is to take advantage of it. Some applications may actually desire a narrow bandwidth. For example, closely packed antennas operating at slightly different frequencies would want a very narrow bandwidth to prevent crosstalk between the antennas.

5.1.2 Applications to Consider

The main strengths of the MEMS resonator are its small size and ease of integration into current circuit fabrication processes. Two application areas that capitalize on these strengths are phase shifting and miniature integrated antennas.

Phase Shifting

The result of my simulation indicate that a MEMS resonator-based phase shifting element can produce a given phase shift of a signal through a much smaller physical size than is currently possible. However, the behavior of a chain of resonators has not been measured. It is unclear if the fabrication process is uniform enough to create several resonators that will behave the same way, which would be necessary for an ideal phase shifter. Future work should explore the phase shifting behavior by

actually constructing a chain of several MEMS resonators in the series configuration and determining if the behavior is consistent with the model.

Filters

The MEMS resonators present a complex input-output relationship. If this relationship could be optimized with the use of several other resonators or circuit elements, interesting RF filters could be constructed. Additionally, due to the small size of the resonators, this filter may be much smaller than other filters that are currently used.

Antennas

Sever potential methods through which the use of MEMS could create an improved patch antenna were discussed. The most promising applications include the reduction of the size of the patch and the conversion of the ground plane to a perfect magnetic conductor or a high impedance material.

A patch antenna my be miniturized through the use of MEMS due to their improved phase shifting behavior. Future work in this direction would require the fabrication of a patch antenna loaded by these resonators. Or, possibly equivalently, an array of the resonators will be constructed. The resonant radiant behavior of this structure must be analyzed further.

A Perfect Magnetic Conductor (PMC) is a material that suppresses the propagation of electric fields along its surface. The use of this material as a ground plane could increase the efficiency of antennas while decreasing their size. Future work towards this goal would require measurements of the behavior of the resonator and the coplanar structure when excited by a propagating electric field from a direction outside of the characteristic plane of the structure. Detailed measurements of the interaction of several resonators in this situation would also be valuable.

Appendix A

Mathematical Work

This Appendix contains mathematical work that is important for the work of this thesis, but was not necessary to include in the main body.

A.1 Calculating the Impedance of a Coplanar Transmission Line

A coplanar waveguide (CPW) is a transmission line that consists of three lines of conductors, that all lie on the same plane. The middle line is a signal line while the outer two are used for the ground. The use of CPWs has become common, as their geometry allows for easy connection of lumped components, no drilling is needed to reach the ground plane, and the transition to other coplanar lines is simplified. Many circuit elements, such as our resonators, are coplanar in nature, so the move to CPW is natural. The performance of CPWs is comparable, and may sometimes exceed that of parallel-plate transmission lines in terms of guide wavelength, dispersion, and losses. However, CPWs have disadvantages of parasitic modes, lower power-handling capability, and field nonconfinment. [13]

Because the geometry of the CPW does not produce the electromagentic fields like those in parallel-plate transmission lines, it is not easily modeled as the lumped circuit elements that are used for most analysis. This exercise would require the

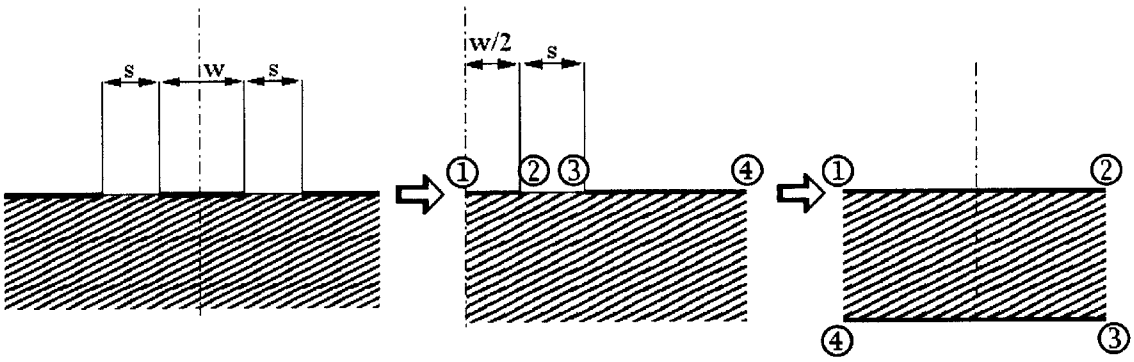

Figure A-1: Demonstration of the conformal mapping of a Coplanar Waveguide to a parallel-plate waveguide. Based on images from [20] and [13].

solution to Laplace's equation in two dimensions. Instead, we use conformal mapping to convert the CPW to a parallel-plate transmission line in order to extract these parameters. The following analysis is taken from [13] and [7].

Figure A-1 outlines the basic method that we will use. We first assume that all dielectric boundaries can be replaced with magnetic walls. This assumption is valid because most of our electric field lines run along these boundaries. After placing the magnetic walls, each side of the wall can be analyzed separately for the distributed capacitance. The resulting line capacitance will then be the parallel combination of these two capacitances.

The conformal function to map the CPW to a parallel-plate capacitor is:

$$w = \int_{z_0}^{z} \frac{dz}{\sqrt{(z - W/2)(z - W/2 - s)}}$$

In the above equation, w is the new characteristic axis and z was the old. The area of the capicitor plate obtained by carrying out the integration. The result is:

$$\frac{\bar{12}}{\bar{23}} = \frac{K(k_1)}{K'(k_1)}$$

In this equation, $\bar{ab}$ indicates the distance between points a and b in the w-plane, and the geometric component, $k_1 = \frac{W}{W+2s}$. $K(k_1)$ and $K'(k_1)$ are the complete elliptic integral of the first kind and its compliment, respectively. These two are related by:

$$K'(k) = K(k') \qquad \text{with } k' = \sqrt{1-k^2}$$

Therefore the value of the ratio $\frac{K}{K'}$ can be approximated by:

$$\frac{K(k_1)}{K'(k_1)} = \begin{cases} \frac{\pi}{\ln 2\frac{1+\sqrt{k'}}{1-\sqrt{k'}}} & \text{for} \quad 0 \le k \le \frac{1}{\sqrt{2}} \\ \frac{\ln 2\frac{1+\sqrt{k}}{1-\sqrt{k}}}{\pi} & \text{for} \quad \frac{1}{\sqrt{2}} \le k \le 1 \end{cases} \tag{A.1}$$

The capacitance of the top half of the CPW structure (which becomes the air-filled capacitor) is:

$$C_a = 2\epsilon_0 \frac{K(k_1)}{K'(k_1)} \tag{A.2}$$

The capacitance of the lower, dielectric-filled half is:

$$C_d = 2\epsilon_0\epsilon_r \frac{K(k_1)}{K'(k_1)} \tag{A.3}$$

The total capacitance of the line is $C_a + C_d$ and the simplest form of the effective permittivity, ignoring metallization thickness and dispersion is:

$$\epsilon_{re} = \frac{\epsilon_r + 1}{2} \tag{A.4}$$

If we wish to include dispersion, we obtain the frequency dependent formula for ϵ_{re} from [14]:

$$\sqrt{\epsilon_{re}(f)} = \sqrt{\epsilon_{re}(0)} + \frac{\sqrt{\epsilon_r} - \sqrt{\epsilon_{re}(0)}}{1 + G\left(\frac{f}{f_{TE}}\right)^{-1.8}} \tag{A.5}$$

where:

$$\begin{aligned} G &= e^{u\cdot\ln\left(\frac{W}{s}\right)+v} \\ u &= 0.54 - 0.64p + 0.015p^2 \end{aligned}$$

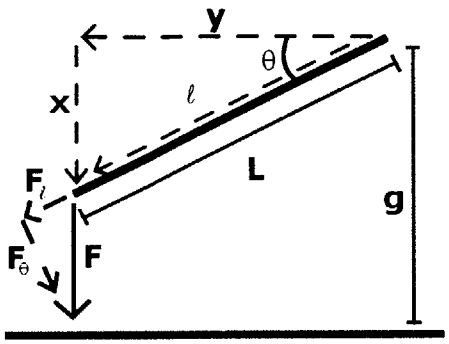

Figure A-2: A force diagram for a cantilever.

$$\begin{aligned} v &= 0.43 - 0.86p + 0.54p^2 \\ p &= \ln\left(\frac{W}{h}\right) \end{aligned} \tag{A.6}$$

And f_{TE} is the cutoff frequency of the TE_0 mode:

$$f_{TE} = \frac{c}{4h\sqrt{\epsilon_r - 1}}$$

From the conformal mapping, the impedance of the CPW is given by that of the capacitor [22]:

$$Z = \frac{\sqrt{\epsilon_{re}}}{cC}$$

Where c is the speed of light in free space and C is the capacitance per unit length of the line from the sum of Equations A.2 and A.3. This expression can be expanded to obtain:

$$Z = \frac{30\pi}{\sqrt{\epsilon_{re}}} \cdot \frac{K'(K_1)}{K(k_1)} \tag{A.7}$$

A.2 Calculating the Torque on a Cantilever

In this section, I calculate the torque that is acting on an electrostatically actuated MEMS cantilever. To find an expression for the torque, one first calculates the torque due to one small piece of the bar as a function of theta and its length along the bar.

Then the force is summed for all the pieces along the bar to get the total torque.

To begin this analysis, we start with the equation for the force on the plates of a capacitor.

$$F = \frac{V^2}{2}\frac{dC}{dx} \tag{A.8}$$

In this equation, the dimension x is the distance between the plates of the capacitor. Similarly, in our model shown in Figure A.2 x is the dimension that characterizes the distance between the cantilever and the driving transmission line. This transmission line becomes the bottom plate of our capacitor, while the moving bar is the top plate. The parameter g is the distance between the cantilever and the transmission line when θ is zero.

We can model each small section of the bar as a parallel-plate capacitor and neglect the fringing fields. If we do this, the capacitance of a segment of the bar with width w and length dl is:

$$C = \frac{\epsilon_0 w dl}{g - x} = \frac{\epsilon_0 w dl}{g - l\sin\theta} \tag{A.9}$$

Using this equaion, we determine the incremental change in capacitance due to a change in θ:

$$\frac{dC}{d\theta} = \frac{\epsilon_0 w l\cos\theta}{(g - l\sin\theta)^2} dl \tag{A.10}$$

To find the force, we substitute into Equation A.8:

$$\begin{aligned} F &= \frac{V^2}{2}\frac{dC}{d\theta}\frac{d\theta}{dx} \\ &= \frac{V^2}{2}\frac{\epsilon_0 w l\cos\theta}{(g - l\sin\theta)^2} dl\frac{d\theta}{dx} \end{aligned}$$

Then, using trigonometry, we know that:

$$x = l\sin\theta \qquad \text{and therefore,} \qquad \frac{dx}{d\theta} = l\cos\theta$$

And we can substitute to determine the force:

$$F = \frac{V^2}{2}\frac{\epsilon_0 w}{(g - l\sin\theta)^2}dl \tag{A.11}$$

The torque, however, is the force perpendicular to the bar, multiplied by the distance from the pivot. This is obtained as follows:

$$\begin{aligned} \tau_{dl} &= F_\perp l = F \cdot l = F\cos\theta l \\ &= \frac{V^2\epsilon_0 w}{2}\frac{l\cos\theta}{(g - l\sin\theta)}dl \end{aligned} \tag{A.12}$$

By integrating Equation A.12 along the length of the cantilever, we obtain the total torque:

$$\begin{aligned} \tau &= \int_l \tau dl = \int_0^L \frac{V^2\epsilon_0 w}{2}\frac{l\cos\theta}{(g - l\sin\theta)}dl \\ &\vdots \\ &= \frac{V^2\epsilon_0 w\cos\theta}{2\sin^2\theta}\left(\frac{L\sin\theta}{g - L\sin\theta} - \ln\frac{g}{g - L\sin\theta}\right) \end{aligned} \tag{A.13}$$

Bibliography

[1] What is mems technology? http://www.memsnet.org/mems/what-is.html.

[2] James Baker-Jarvis, Eric J. Vanzura, and William A. Kissick. Improved technique for determining complex permittivity with the transmission/reflection method. *IEEE Transactions on Microwave Theory and Techniques*, 38(8):1096–1103, August 1990.

[3] C. Caloz, C.-C. Chang, and T. Itoh. Full-wave verification of the fundamental properties of left-handed materials in waveguide configurations. *Journal of Applied Physics*, 90(11):5483–5486, 2001.

[4] D.W. Carr, S. Envoy, L. Sekaric, H.G. Craighead, and J.M. Parpia. Parametric amplification in a torsional microresonator. *Applied Physics Letters*, 77(10):1545–1547, September 2000.

[5] Kieth R. Carver and James W. Mink. Microstrip antenna technology. *IEEE Transactions on Antennas and Propagation*, AP-29(1):2–24, January 1981.

[6] L. J. Chu. Physical limitations of omni-directional antennas. *Journal of Applied Physics*, 19:1163–1175, December 1948.

[7] Robert E. Collin. *Foundations for Microwave Engineering.* IEEE Press, New York, second edition, 2001.

[8] George V. Eleftheriades, Ashwin K. Iyer, and Peter C. Kremer. Planar negative refractive index media using periodically l-c loaded transmission lines. *IEEE*

Transactions on Microwave Theory and Techniques, 50(12):2702–2712, December 2002.

[9] S. Envoy, D.W. Carr, L. Sekaric, A.Olkhovets, J.M. Parpia, and H.G. Craighead. Nanofabrication and electrostatic operation of single-crystal silicon paddle oscillators. *Journal of Applied Physics*, 86(11):6072–6077, December 1999.

[10] H. Ford. *Advanced Mechanics of Materials.* Longmans, Green, London, 1963.

[11] D.K. Ghodgaonkar, V.V. Varadan, and V.K. Varadan. Free-space measurement of complex permittivity and complex permeability of magnetic materials at microwave frequencies. *IEEE Transactions on Instrumentation and Measurement*, 39(2):387–394, April 1990.

[12] R.B. Greegor, C.G. Parazzoli, K.Li, and M.H. Tanielian. Origin of dissipative losses in negative index of refraction materials. *Applied Physics Letters*, 82(14):2356–2358, April 2003.

[13] K.C. Gupta, Ramesh Garg, Inder Bahl, and Prakash Bhartia. *Microstrip Lines and Slotlines.* Artech House, Boston, second edition, 1996.

[14] G. Hasnain, A. Dienes, and J.R. Whinnery. Dispersion of picosecond pulses in coplanar transmission lines. *IEEE Transactions on Microwave Theory and Techniques*, MTT-34(6):738–741, June 1986.

[15] Luke A. Hohreiter. The effects of mechanical coupling on the electrical impedance of mems resonators for uhf filter applications, 2004.

[16] Ahmad Hoorfar, John McVay, Jinhui Zhu, and Hui Huang. Novel electrically small antennas and metamaterial high impedance substrates. Technical report, Office of Naval Research, December 2005.

[17] Holger H. Hoos. On the run-time behaviour of stochastic local search algorithms for sat, 1999.

[18] Lung-Hwa Hsieh and Kai Chang. Equivalent lumped elements g, l, c, and unloaded q's of closed- and open-loop ring resonators. *IEEE Transactions on Microwave Theory and Techniques*, 50(2):453–460, February 2002.

[19] Sheldon H. Jacobson and Enver Yücesan. Analyzing the performance of generalized hill climbing algorithms. *Journal of Heuristics*, 10:387–405, 2004.

[20] S. Jahn, M. Margraf, V. Habchi, and R. Jacob. Qucs technical papers: Coplanar waveguides. http://qucs.sourceforge.net/tech/node55.html.

[21] J. Kang. Piezoelectric mems resonator characterization and filter design, March 2004.

[22] Paul R. Karmel, Gabriel D. Colef, and Raymond L. Camisa. *Introduction to Electromagnetic and Microwave Engineering.* Wiley-Interscience, first edition, December 1997.

[23] Gullu Kiziltas, Dimitris Psychoudakis, John L. Volakis, and Noboru Kikuchi. Topology design optimization of dielectric substrates for a bandwidth improvement of a patch antenna. *IEEE Transactions on Antennas and Propagation*, 51(10):2732–2743, October 2003.

[24] Young-Hag Koh, Angela Kapp, and John W. Halloran. Thermoplastic green machining for textured dielectric metamaterials for miniaturized patch antennas. Technical report, DARPA.

[25] Jin Au Kong. *Electromagnetic Wave Theory.* EMW Publishing, 2000.

[26] Anthony Lai, Tatsuo Itoh, and Cristophe Caloz. Composite right/left-handed transmission line metamaterials. *IEEE Microwave Magazine*, pages 34–50, September 2004.

[27] Rong Liu, Brad Panden, and Kimberly Turner. Mems resonators that are robust to process-induced feature width variations. *Journal of Micorelectromechanical Systems*, 11(5):505–511, October 2002.

[28] Hossein Mosallaei and Kamal Sarabandi. Antenna miniaturization and bandwidth enhancement using a reactive impedance substrate. *IEEE Transactions on Antennas and Propagation*, 52(9):2403–2414, September 2004.

[29] H.O. Moser, B.D.F. Casse, O. Wilhelmi, and B.T. Shaw. Terahertz response of a microfabricated rod-split-ring-resonator electromagnetic metamaterial. *Physical Review Letters*, 94(063901):1–4, 2005.

[30] J.B. Pendry. Negative refraction makes a perfect lens. *Physical Review Letters*, 85(18):3966–3969, 2000.

[31] J.B. Pendry, A.J. Holden, D.J. Robbins, and W.J. Stewart. Magnetism from conductors and enhances nonlinear phenomena. *IEEE Transactions on Microwave Theory and Techniques*, 47(11):2075–2087, November 1999.

[32] J.B. Pendry, A.J. Holden, W.J. Stewart, and I. Youngs. Extremely low frequency plasmon in metallic mesostructures. *Physical Review Letters*, 76(25):4773–4776, June 1996.

[33] David M. Pozar. *microwave Engineering.* John Wiley and Sons, third edition, 2005.

[34] R.A. Shelby, D.R. Smith, and S. Schultz. Experimental verification of a negative index of refraction. *Science*, 292(5514):77–79, 2001.

[35] D.R. Smith, Willie J. Padilla, D.C. Vier, S.C. Nemat-Nasser, and S. Schultz. Composite medium with simultaneously negative permeability and permittivity. *Physical Review Letters*, 84(18):4184–4187, May 2000.

[36] D.R. Smith, S. Schultz, P. Markos, and C.M. Soukoulis. Determination of effective permittivity and permeability of metamaterials from reflection and transmission coefficients. *Physical Review B*, 65(195104):1–5, April 2002.

[37] D.R. Smith, D.C. Vier, N. Kroll, and S. Schultz. Direct calculation of permeability and permittivity for a left-handed metamaterial. *Applied Physics Letters*, 77(14):2246–2248, October 2000.

[38] V. G. Veselago. The electrodynamics of substances with simultaneously negative values of ϵ and μ. *Soviet Physics Uspekhi*, 10(4):509–514, January 1968.

[39] K.J. Webb, M. Yang, D.W. Ward, and K.A. Nelson. Metrics for negative-refractive-index materials. *Physical Review*, September 2004.

[40] Richard W. Ziolkowski. Design, fabrication, and testing of double negative metamaterials. *IEEE Transactions on Antennas and Propagation*, 51(7):1516–1529, July 2003.

[41] Richard W. Ziolkowski and Fabrice Auzanneau. Passive artificial molecule realizations of dielectric materials. *Journal of Applied Physics*, 82(7):3195–3198, October 1997.